UNIVERSITY OF TWENTE.

Faculty of Engineering Technology

Investigation of delamination crack under vibration fatigue exploiting simulation aided dynamic testing in digital environment

MSc. Thesis Mechanical Engineering

Frank R. Oosterveld, s1421018

July 2021

191199198

Supervisor UT:
Dr. Dario Di Maio

Dynamics Based Maintainance
Faculty of Engineering Technology
University of Twente
Horst Complex N138
P.O. Box 217
7500 AE Enschede
The Netherlands

Summary

This thesis work examines the damage propagation in composite laminates under vibration fatigue. Throughout the chapters, an overview of fatigue behaviour of composites will give an insight into the challenges of testing composites and a complete theoretical background will allow the reader to understand the method development. Nowadays, composite materials are used in all structural components of automotive, aerospace and, soon, space industry. However, fatigue is still an open challenge for structural components because of its underlying complex physics. One of the major challenges of testing in composites is to overcome the extremely time consuming testing procedure. Standard fracture mechanic tests under ASTM standards use a superposition of mode-I and mode-II to take into account the mode mixity ratio in real conditions. However, aerospace loading environments are dynamic and not quasi-static as in the testing practices. As an alternative, vibration testing is proven to be effective in monitoring the onset of delamination and its propagation. Experimental measurements underscore that the delamination growth can be described by the linear relationship that the vibration response phase has with the number of excitation cycles. Yet, these measurements are time consuming, as CT scans and microscopes are being used to identify the crack length. This leads to the exploitation of numerical models about the observed experimental behaviour.

Previous numerical simulations did not take into account the friction forces developed at the interfaces of the delamination. One of the main objectives is to construct a remastered finite element model including contact elements to simulate the friction effects. Consequently, a framework is developed to investigate the forces at the crack tip acting at two ends of the delamination, based on steady-state dynamics instead of transient analysis, allowing a rapid simulation process. With use of this novel numerical framework, the forces determining the failure mode-I and mode-II are investigated.

Due to the inclusion of the contact area in the FE model, a different numerical mode-mixity is present for the 'crack-opening' and 'crack-closing' deflection of the fully reverse cycle. For the crack-opening deflection, the $\mathrm{G_I}$ (the mode I bending contribution to crack opening) has the most dominant influence in the total SERR, $\mathrm{G_T}$. However a combination of both $\mathrm{G_I}$ and $\mathrm{G_{II}}$ (the mode II shear contribution to crack opening) results in the crack growth. For the crack-closing deflection, it can be concluded that the $\mathrm{G_{II}}$ does not have any contribution to the crack length. This means that, for opening the crack, all the strain energy comes from the in-plane shear sliding mode.

Finally, the numerical analysis constructs a relationship between the SERR and the vibration response phase over the total delamination length. A novel calibration factor/function is introduced to convert the measured response phase into the equivalent Strain Energy Release Rate. This results a broader understanding in the physical phenomena underneath the delamination crack under vibration fatigue will be gained. By obtaining a more profound understanding in the physics, the results of the experiments can be analyzed in a better way. This thesis represents a solid starting point to elaborate on fracture mechanics investigation, especially for aerospace applications where time saving, efficient and innovative techniques are required.

Nomenclature

$\bar{U}$	Magnitude of displacement
ϵ	Strain in material
η	BK-powerlaw coefficient
λ	Eigenvalue
μ	Friction Coefficient
ν	Poisson ratio
ω_{exc}	Excitation frequency
ω_n	Resonance frequency
ϕ	Dynamic Phase of response
σ	Stress in material
ζ	Damping ratio
a	Crack Length
C	Intercept of Paris-Erdogan law
c	Damping coefficient
$CFRP$	Carbon Fibre Reinforced Plastic
d	Severity level
DCB	Double Cantilever Beam
DNS	Double Notched Shear
E	Young's Modulus
F	Force
f	Fracture criterion
$F_{initial}$	Initial force
FEA	Finite Element Analysis
FEM	Finite Element Method
FRF	Frequency Response Function
G	Receptance
G	Shear Modulus

G Strain Energy Release Rate (SERR)

G_I Mode I (Opening component) of SERR

G_{II} Mode II (Shearing component) of SERR

$G_{T,c}$ Total critical Equivalent SERR

G_T Total equivalent SERR

h Width of the numerical model

I Second moment of inertia

k Stiffness

L Length of specimen

LDV Laser Doppler Vibrometer

$LEFM$ Linear Elastic Fracture Mechanics

m Mass

N Number of cycles

n Slope of Paris-Erdogan law

ODS Operating Deflection Shape

R Stress Ratio

SBS Short Beam Shear

$SDOF$ Single Degree Of Freedom

SSD Steady State Dynamics

t Time

U Displacement

U Elastic Energy

U_i Imaginary component of displacement

U_r Real component of displacement

u_{2l} Horizontal displacment in l

U_{ref} Displacement of reference node

UD Unidirectional

w_{2l} Vertical displacement in l

X_{1l} Horizontal force at node l

$y(t)$ Vertical motion

Z_{1l} Vertical force at node l

Acknowledgements

First and foremost, I would like to express my gratitude towards all who enabled my graduation assignment. Due to COVID-19 we had to face various difficulties, but aside many other names, I would like to thank my daily supervisor at the University of Twente: Dr. Di Maio who gave me the opportunity to continue my studies and be a part of this project. I really admire Dario's efforts to push through and give excellent guidance throughout the process. For giving me the trust and freedom in my daily activities. That is something I appreciate a lot.
Then I would like to thank everybody from the Dynamics Based Maintainance research chair organized by Dr. Ir. R. Loendersloot, who all listened to my updates and provided constructive feedback.
Finally I would like to thank all my friends and family for all the constructive discussions, support and guidance.

Frank Oosterveld

Signature 8 July 2021

Contents

Chapter 1

Introduction

1.1 Aim of the Research

Nowadays, composite materials are used in all structural components of automotive, aerospace and, soon, space industry. Advanced composites give designers of aircrafts an expanded toolbox of materials. These composites are currently used in structural components such as clips and brackets, but are under trial and consideration for primary structural components such as fuselage panels, wing boxes and stringers [1]. The parts are highlighted in figure 1.1.

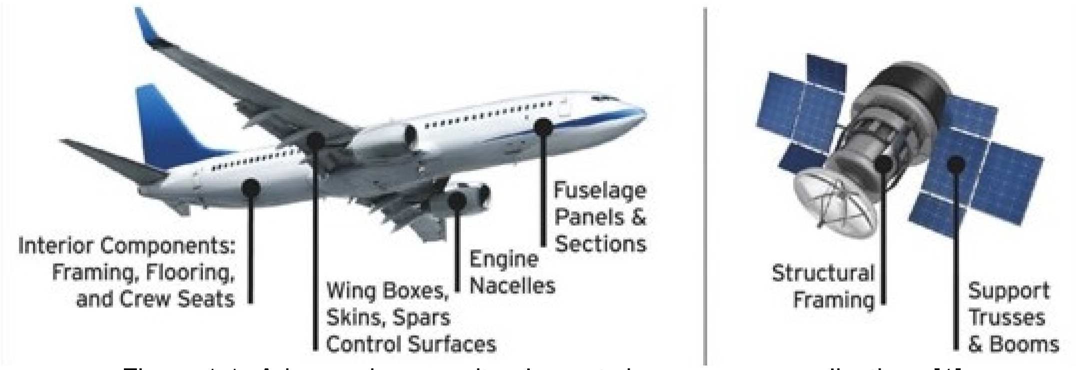

Figure 1.1: Advanced composite elements in aerospace applications [1]

In addition to commercial aircraft, composite materials also find use in demanding satellite applications. The component's light weight and high stiffness is ideal for the launch vehicle and the payload [1]. Composites will soon cross the cost-benefit viability threshold for widespread use in civil and space divisions. However, fatigue is still an open challenge for structural components because of its underlying complex physics.

One of the major challenges of fatigue testing of composites is to overcome the extremely time consuming testing procedure. In standard fatigue tests, the loading frequency is kept below a few dozen of cycles per seconds. There is one reason for doing so; to avoid an excessive self-heating [2]. However, understanding the fatigue behaviour of composite materials is fundamental for efficient structural designs.Yet, despite the acquisition of large collections of mechanical property data, the ability to predict the structural integrity of a damaged composite subjected to mechanical stresses and hostile environment remains restricted [3].

Nowadays, the test, analysis and numerical modelling of mechanical failure of materials is very well established. The fracture mechanics characterization is done by standard tests using hydraulic machines for all materials. For instance, the fatigue damage growth is carried out using unidirectional laminates with a delamination onset longer than 50 mm. The type of test is a Double cantilever beam (DCB) test and it is used for characterising the mode-I bending failure following the ASTM standard ASTM D6115 [4]. The mode-II shearing failure under fatigue is tested with use of the Short Beam Shear (SBS) test or the Double Notched Shear (DNS) test. characterized by different standard; respectively ASTM D2344 [5] and ASTM D3846 [6]. Eventually, both mode-I and mode-II are superimposed to take into account the mode mixity ratio in real conditions.

However, aerospace loading environments are dynamic and not quasi-static as in the testing practices. Sometimes it is possible to uncover hidden relationships by studying the overall phenomenon. If natural vibration is one of the main players in the fatigue life of some components, natural vibrations should be induced to study the fatigue behaviour of those components. Dynamic loads, the ones right beyond the first resonant mode of vibration can lead to self-heating conditions which make the assessment of the material behaviour time-temperature dependent. Therefore, those are limited to very low rates. However, the true nature of the internal forces under dynamic loads leading to fatigue might not be as simple as the linear superimposition summation. Hence, one could question why the natural vibration of the response cannot be evaluated to observe how forces at the crack tip operates.

Past researches have highlighted that the use of vibration testing is very effective in monitoring the onset of delamination and and its propagation. Those researches showed that that the delamination growth can be described by the linear relationship that the vibration response phase has got with the number of excitation cycles. Experimental measurements by CT scan underscore such linear relationship [7]. Despite the fact that high frequency fatigue testing is characterised by multiple advantages, certain limitations also are also present. It is easy to understand how challenging it could be to capture certain parameters (e.g. continuous damage accumulation) during high frequency excitation experimental testing. In previous research, extensive X-ray CT scans or microscopic investigation are needed to identify the crack length [2]. For this reason, numerical models can be exploited, alongside the experimental investigation, to enhance our understanding about the observed experimental behaviour.

Basic numerical analyses have calculated the Strain Energy Release Rate (SERR) over the number of cycles and observed how the SERR relates to the vibration phase dropped measured during tests [2]. The phase-drop is more susceptible to change then the frequency, providing a higher sensitivity; smaller changes in the stiffness can be observed. These dynamic parameters can be measured continuously during experimental vibration testing. Unfortunately, those simulations did not take into account the friction forces developed at the interfaces of the delamination. That means that true contact could not be taken into account. The non-linear friction effects are thus neglected, while they may play an important role in the shear contribution to the crack propagation. The reason for not including this contribution was the complicated layup geometry consisting of cross-ply with some ply-drops where the fatigue delamination was observed.

One of the ambitions of this research is to understand what could be the contribution of the friction forces which are nearly impossible to measure by experiments. The past researches developed a crack-growth methodology based on steady-state dynamics instead of transient, which allowed a rapid simulation process [7].

With use of the numerical models, the forces determining the failure mode-I and mode-II can be investigated. This results in the main research objective:

"What are the contributions of failure modes I and II to the delamination growth under vibration loading conditions and how can this be modelled efficiently by a new numerical model including contact elements to simulate friction effects in the delamination area?"

As already said, the research will start from what past researchers left unchallenged. However, the sample design was simplified from cross-ply with ply drops to cross-ply with ply cut. The new designed allowed the crack to develop from the surface transverse up to a point when it becomes interlaminar, thus forming a sort of T-shape crack. Such crack profile under fully reversible loading conditions will show a closure and opening depending on the deflection shape. Furthermore, that crack is placed away from the maximum bending locations.

Under such conditions, the research will primarily develop a framework to investigate the forces at the crack tip acting at two ends of the delamination. That first objective will show how an experimental test can be broken down by finite element analysis to allow such investigation.

Upon the achievement of the first objective, the second one will be to investigate the magnitude of the $\mathrm{G_I}$ and $\mathrm{G_{II}}$ for both opening and closing delamination. What are the differences in mode mixity between the crack-opening and crack-closing case? The goal is to understand the SERR changes for the positive and negative cycle of vibrations.

Finally, the numerical analysis will attempt to construct a relationship between the SERR and the vibration response phase over the total delamination length. The objective of this final attempt lies on the type of experiments carried out in the past, such as tracking the response phase during the fatigue tests. Hence, one would like to know if the response phase measured experimentally can be converted by some sort of calibration factor/function into the equivalent SERR.

1.2 Report organization

In Chapter 2, an extensive literature review will give an introduction to the reader to the world of composites from two different points of view: the one of the dynamic expert and the one of the material scientist. Sections on fatigue of composite materials are followed by sections presenting an overview of the dynamic tools that are used in the thesis, with a description of their experimental and modelling aspects.

Then, Chapter 3 presents the new FE model, how a novel numerical model including frictional forces in the delaminated area is build.

Additionally, Chapter 4 describes a new FE modelling framework; how this new model can be used in a crack-growth modelling method. A strategy is adopted in tackling various problems in dynamic testing in digital environment.

Results from several data sets acquired with that new FE method were enlightening for the implementation of the new procedure. In Chapter 5, the crack modelling method has been applied and the delamination is captured for the two cases of the fully reversed cycle: the crack-opening and crack-closing deflection.

Furthermore, the results are further analyzed, correlating the dynamic parameters to the crack length. It is proved that the dynamic properties i.e. response phase is much more sensitive in capturing damage development and structural degradation than the more commonly used resonance frequency decay. Then, it shows the differences of the mode mixity for the two cases. It shows that for the low severity level the crack-closing case is not influenced by mode I, while the crack-opening is. These correlations make it possible to relate the SERR to the phase-drop. Which makes it possible to predict the SERR by means of a very novel calibration factor. This means that by measuring the difference in phase-drop - which one can do during the experiments; one can calculate the real-time SERR value by multiplication with a new calibration factor.

Finally, in Chapter 6, the summary of the achievements are reported and the conclusions are drawn, paving the way for future work in Chapter 7.

Chapter 2

Literature research

2.1 An introduction to composites

The advent of the composites as a distinct classification of materials began during the mid-20th century with the manufacturing of multi phase composites such as fiberglass-reinforced polymers. Although multi phase materials, such as wood, seashells and even alloys such as steel had been known for millennia, recognition of this novel concept of combining together led to the identification of composites as a new class that was separate from the familiar metals, ceramics, and polymers [8]. We now realize that this concept of multi phase composites provides exciting opportunities for designing and exceedingly large variety of materials with property combinations that cannot be met by any of the monolithic conventional metal alloys, ceramics and polymeric materials [8]. Many composite materials are composed of just two phases; one is termed the matrix, which is continuous and surrounds the other phase, often called the dispersed phase. Within composites, a classification can be made between various composite types: particle-reinforced, fiber-reinforced and structural composites.

2.1.1 Fiber reinforced plastics

Technologically, the most important composites are those in which the dispersed phase is in the form of a fiber. Fiber-reinforced composites are familiar for their high strength and/or stiffness on a weight basis. These characteristics are expressed in terms of specific strength and specific modulus parameters. The mechanical characteristics of a fiber-reinforced composite depend not only on the properties of the fiber, but also on the degree to which an applied load is transmitted to the fibers by the matrix phase [8]. Important to the extent of this load transmittance is the magnitude of the inter facial bond between the fiber and the matrix phases.

2.1.2 Laminar composites

A laminar composite is composed of two-dimensional sheets or panels that have a preferred high-strength direction, which is found in wood and continuous Fiber Reinforced Plastics (FRPs). Within FRPs there are two main classifications: thermoset and thermoplastic FRP. The primary difference between the two is that thermoset is a material that strengthens when heated, but cannot be remolded or heated after the initial forming, while thermoplastics can be reheated, remolded, and cooled as necessary without causing any chemical changes[9].

The layers are stacked in a stacking sequence and subsequently cured together such that the orientation of the high-strength direction varies with each successive layer, as seen in figure 2.1 [8]. A variety of fabrics is available, where a unidirectional (UD) layup is one in which the majority of fibres run in one direction only. Unidirectional carbon fiber fabric is a type of carbon reinforcement that is non-woven and features all fibers running in a single, parallel direction. A cross-ply laminate contains an arbitrary number of these plies, each with a fiber orientation of either 0° or 90°, which can be either symmetric or antisymmetric [10]. When these cross-plies are stacked such that the orientation of the fibers in the lay-up are balanced, resulting in constant strength and stiffness of the material regardless of the direction in which it is loaded, then the FRP laminates have quasi-isotropic properties [10].

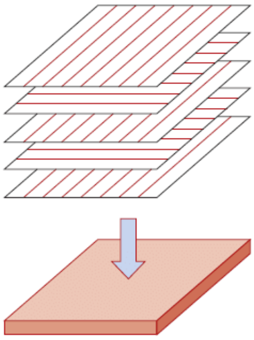

Figure 2.1: Stacking of successive oriented fiber-reinforced UD plies for a quasi-isotropic laminar cross-ply composite [8]

.

2.2 Fatigue behavior in composite materials

Fatigue is a form of failure that occurs in structures subjected to dynamic and fluctuating stresses. Under these circumstances it is possible for failure to occur at a stress level considerably lower than the tensile or yield strength for a static load. Fatigue failure is brittle like in nature and even in normally ductile materials. The process occurs by the initiation and propagation of cracks. The fatigue mechanisms in longitudinal composites can be described by the schematic illustration in figure 2.2 . In a greater detail, the delamination after the matrix crack is visualized by a microscopic picture in figure 2.3.

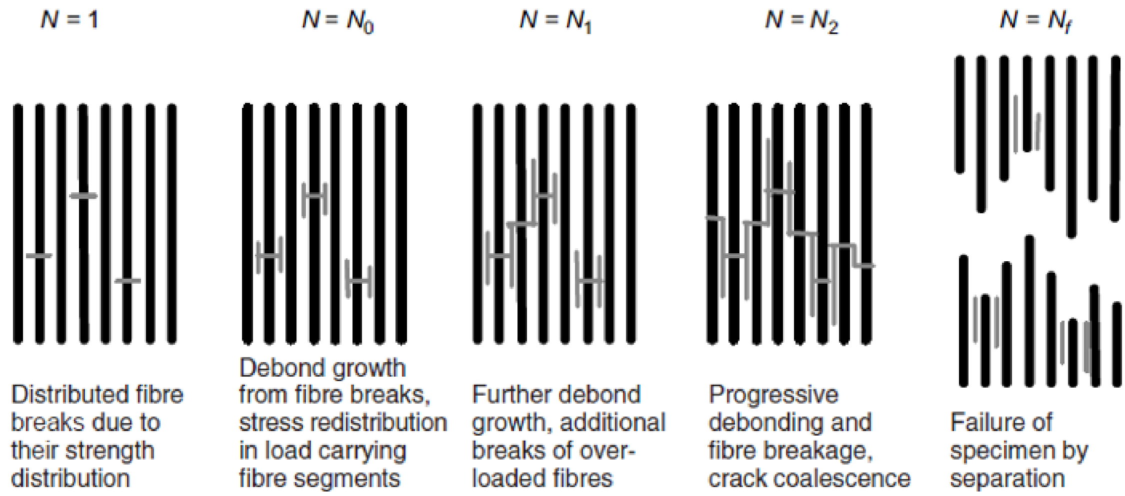

Figure 2.2: Schematic illustration of fatigue damage development until final failure in longtudinal composites, where damage initiates from individual fibre breaks from which longtudinal cracks or debonds [11].

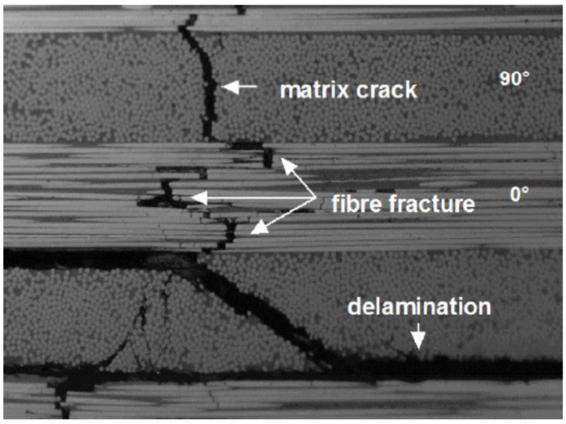

Figure 2.3: Damage mechanisms in CFRP under vibration fatigue [12].

The mechanisms under vibration fatigue are as follows: The brittle fibres have almost always a lower strain to failure than the thermoplastic matrix. Since the fibres have a distribution in strain to failure, some of the fibres will fail at the first application of load. The failure of these fibres will serve as initiation points for further damage development. Longitudinal damage grows by delamination, matrix cracking or yielding, as seen in figure 2.3. These processes are controlled by the matrix or the fibre-matrix interface. As the longitudinal cracks grow, the local stress profiles in the neighboring fibres will continually change. An overload in a weak part of a nearby fibre may thus result in a new fibre break [11]. Longitudinal cracking can then continue at a higher rate, and result in further fibre breakage and crack growth in a self-escalating manner until the point of final failure. The matrix and its interface to the fibres will influence the fatigue life of the composite, since they control the progressive mechanism [11].

2.2.1 Crack initiation

The definition of damage initiation is one of the most discussed topics in fatigue behaviour of components. It is widely agreed that the nucleation of damage in a pristine component can be a large part of its total fatigue life, but unfortunately its characteristic features are particularly difficult to understand and therefore to predict. For this reason, the crack initiation is usually related to a subjective critical crack dimension [2]. As the definition of crack initiation is not unique for homogeneous materials, such as metals, it is even harder to find a general definition of initiation for composite materials, where damage is identified by the complex status of the material rather than by a single crack [2]. The definitions of damage initiation range from the first nucleation of a transverse crack in an off-axis ply by Reifsnider's [13] to more practical definitions of initiation given by Salkind [14] as the time required to form a crack of detectable size. According to Reifsnider's, the damage initiation should be defined as the first nucleation of a transverse crack in an off-axis ply.

However, damage initiation could be interpreted at various levels, from the microscopic molecular observation level to the macroscopic structural observation level. Ciulo and Kachanov [15] demonstrated that there is no direct correlation between the clustering of micro-cracks at the microscopic level and the stiffness reduction at structural level. In fact, as the stiffness reduction is property of the entire structure, it averages the crack distribution over the entire volume, resulting in the method being insensitive to clustering. The clustering could have different effects on the structural behaviour [15]. Then, Lomov et al. [16] considered the damage initiation as the occurrence of a crack that connects many debonded fibres and that can be captured by an increase in energy content of acoustic emissions [16].

On the other hand, O'Brian [17] proposed a new damaged tolerance philosophy for composite materials [17]. O'Brian assumed the existence of matrix cracks throughout the off-axis plies and the onset of delamination being predicted by a SERR threshold. This threshold can be obtained by running several tests at several loads, whereby the onset of delamination is always unstable and easily detectable because of catastrophic change in stiffness [17].

Also, Sims [18] reviewed the fatigue testing methods beginning with the concept of failure criterion for composites. He identified the need for a failure criterion based on loss of stiffness, as recommended by standard procedures , that could vary from 5% to 20% depending on applications [19] [18]. Lastly, May and Hallett introduced the incorporation of damage initiation into a cohesive element model [20]. Here, model calibrations were made for both mode I and mode II (respectively the bending and shearing contribution to the crack opening) on transverse tension fatigue and on damage initiation in shear fatigue [21]. For mode I it was observed that initiation and final failure occurred within a short period of time. Thus it was assumed that initiation corresponded to the actual separation of the specimen in two pieces. For mode II, the Short Beam Shear test and the Double Notched Shear test were evaluated and compared for their potential in providing data for SN-curves to damage initiation. After careful consideration, it was concluded that the Double Notched Shear test was more reliable in determining damage initiation. With all these definitions of crack initiation, it is clear that there is no universal criterion to define the damage initiation [2].

2.2.2 Crack propagation

From the previous section of the initiation stage, it is evident that there is no universal criterion to define the damage initiation. However, when the damage is initiated, its propagation is more profound to understand and predict. From the basis of linear elastic fracture mechanics (LEFM), the crack propagates governed by an energy balance: the strain energy stored at the crack tip is released to create a new surface (i.e. to propagate the crack) when it exceeds the fracture toughness of the material, G_c [2]. The strain energy released per unit of propagated area is called G or Strain Energy Release Rate (SERR) and is defined as follows,

$$G = \frac{\partial U}{\partial A} \tag{2.2.1}$$

Where U is the elastic energy available for the crack to grow and A is the crack area. Therefore, the condition for the crack propagation in a quasi static case is given by,

$$G \leq G_c \tag{2.2.2}$$

In fatigue the condition of Equation 2.2.2 is almost never met, as the severity would break the component in the first few cycles. Instead the Paris-Edogan law is used to relate the stable propagation with the SERR (or the stress intensity factor) using the following equation:

$$\frac{da}{dN} = C\Delta G^m \tag{2.2.3}$$

where da/dN is the crack growth rate, ΔG is the difference in SERR and C and m are material constants. This corresponds to the slope in Regime B of figure 2.4

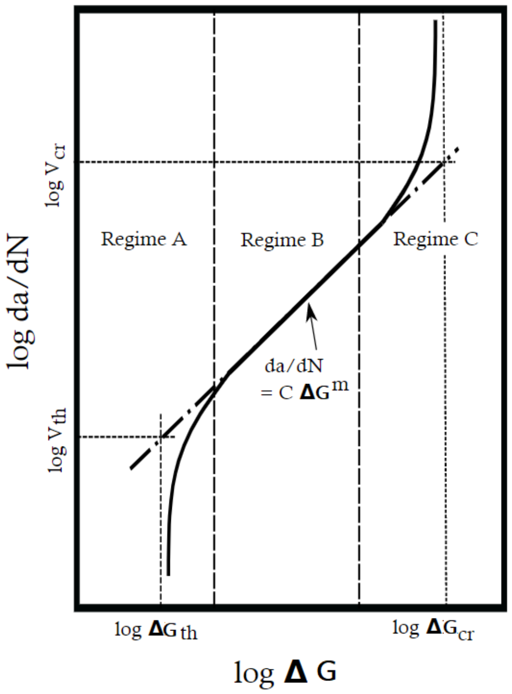

Figure 2.4: Plot of the Paris-Erdogan law [2]

2.2.3 Final failure

As with the initiation of the crack, the definition of final failure is far from being unique. A certain drop in stiffness could be defined as failure even if the component can still carry the load. The reasons for defining failure as a given drop in stiffness, may be found in an excessive deflection under operating conditions as well as in the interference between the natural mode of the component with the vibration modes of the structure where the component is assembled (e.g. a broken blade in a blade disk of a turbine). Another way for defining failure could be as simple as a crack that can be seen by a naked eye. For example, in the case of a coating spray on a particular component, with the only purpose of isolating the component from harsh environmental conditions, a simple surface crack, with no structural consequences, may be considered as failure. In conclusion, it is the designers' responsibility to define failure based on customers' requests and to trade off between an expensive but safe zero damage policy and a cheaper but more challenging damage control policy [2].

2.3 Quasi-static composite material testing

The importance of predicting the total life of a component working within safe operational conditions is well acknowledged by engineers, whose final objective, especially in the aerospace sector, is to design reliable, efficient and lightweight structures. The fail behavior of these structures will form under the effect one (or more) of the characteristic separation modes. These are the opening mode (mode I), the shearing mode (mode II) and the scissoring shear mode (mode III) [12].

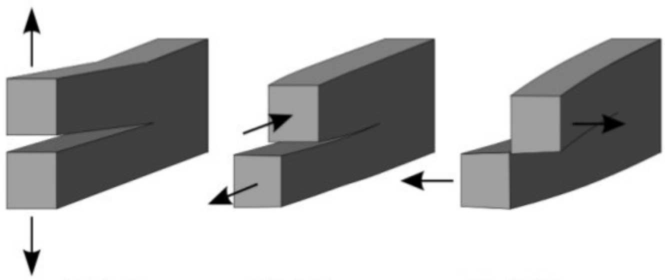

Figure 2.5: Three modes of failure in fracture mechanics [12]

In order to investigate when composites under go failure, a series of mechanical tests should be performed. Currently, Double Cantilever Beam (DCB) tests are being used as a ASTM standard for investigating crack growth under fatigue in aerospace applications. ASTM D6115 is the norm for identifying the crack length under mode-I vibration fatigue of unidirectional CFRP [4]. This test method determines the number of cycles (N) for the onset of delamination growth based on the opening cyclic strain energy release rate (G), using the DCB specimen shown in 2.6. This test method applies to constant amplitude, tension-tension fatigue loading of continuous fiber-reinforced composite materials. [4] This procedure of testing provides estimations of when the composite fails under quasi-static loading conditions. This provides a good understanding for the failure behavior. As a downside, the testing requires a long initial delamination length (a_0), usually in the order of 50 mm.

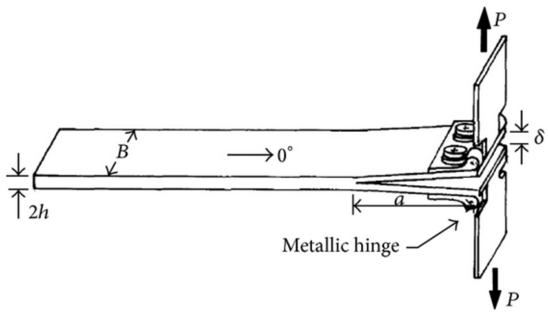

Figure 2.6: DCB specimen under fatigue load [22].

The test method for mode-II testing is performed by the Double Notched Shear test or the Short Beam Shear test [22]. The DNS test covers the determination of the inplane shear strength of reinforced thermosetting plastics in flat sheet form [6]. In-plane shear strength, as determined by this test method, is measured by applying a compressive load to a notched specimen of uniform width. The specimen is loaded edgewise in a supporting jig. A schematic of the specimen used for this test and the supporting jig is shown in figure 2.7. Failure of the specimen occurs in shear between two centrally located notches machined halfway through its thickness and spaced a fixed distance apart on opposing faces [6]. Eventually, both mode-I and mode-II are superimposed to take into account the mode mixity ratio in real conditions vibration fatigue.

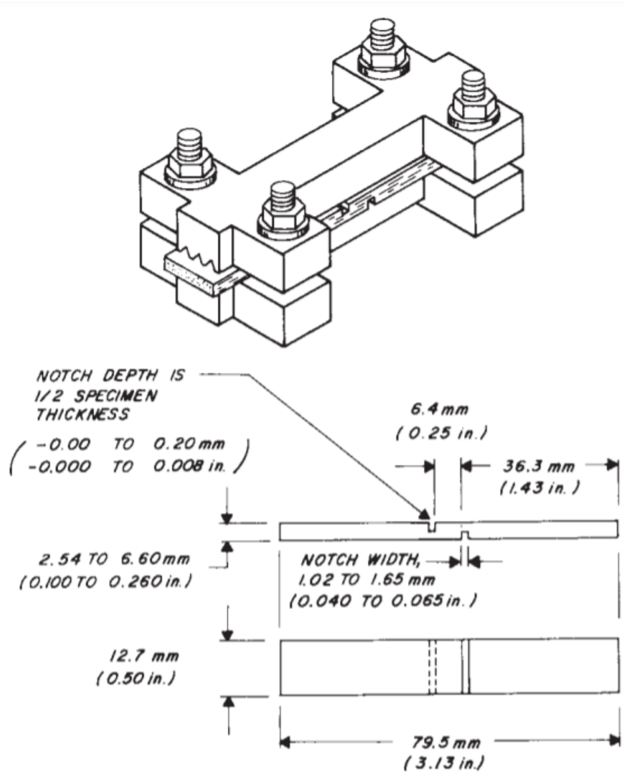

Figure 2.7: Specimen and Loading Jig for In-Plane Shear Test [6].

2.4 Background of structural dynamics

Many years, the aero-engine industry has attempted fatigue trials of components by exploiting resonant conditions. On one hand, the resonant modes offer an immediate benefit in the testing practice by reducing the testing time and by amplifying the response, resulting in a smaller amount of input energy required for achieving large vibration amplitudes. On the other hand, though, vibration testing is complicated by two major factors: the relatively high structural damping and the mechanical impedance mismatch [2]. The study of the dynamic characteristics of a mechanical structure is defined as modal analysis. This application note emphasizes experimental modal techniques, specifically the method known as Frequency Response Function (FRF) testing. The motion of a dynamic structure or system is represented by a set of simultaneous differential equations using some discretization scheme, such as the Finite Element Method (FEM). The dynamic characteristics (dynamic responses, strains, stresses, etc.) of the system can be obtained from these equations using the direct integration methods (Finite Difference Method, Newmark method, for example) in the time domain. Alternatively, these coupled equations of motion may be solved by transforming them into a set of independent (uncoupled) equations by means of a modal matrix. This procedure is the classic meaning of modal analysis. Actually, the procedure of determining the system's modal parameters, including natural frequency, natural mode, damping factor, modal scaling, etc., is also referred to as modal analysis[23].

2.4.1 Steady State Dynamics

Steady State Dynamic (SSD) analysis provides the steady-state amplitude and phase of the response of a system due to harmonic excitation at a given frequency [24]. This means that the structure is already vibrating for a given time, such that fluctuations and irregular behavior of the transient motion can be neglected. The steady state behavior reaches an equilibrium where the amplitude and phase are constant. A typical stress-time plot is shown in Figure 2.8.

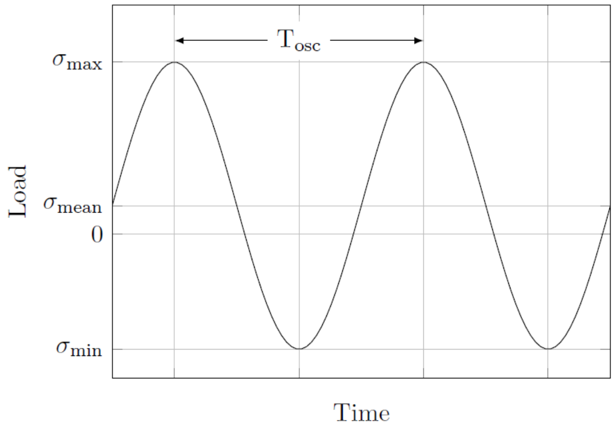

Figure 2.8: Typical sinusoidal loading conditions over time [2].

The loading conditions are usually represented by the following parameters:

$$R = \frac{\sigma_{min}}{\sigma_{max}} \tag{2.4.1}$$

$$f = \frac{1}{T_{osc}} \tag{2.4.2}$$

where σ_{max} and σ_{min} are the maximum and minimum stresses in the component, respectively, T_{osc} is the period of oscillation, R is the stress ratio and f is the oscillation frequency. These parameters are fundamental in the fatigue behaviour of FRP, and they affect the total life, both together and independently. A high loading frequency causes the self-heating of the material, that in some cases reduces the fatigue life. On the other hand, an opportunely high frequency affects the fatigue life by increasing the cycles to failure, as the material stays at high strains for a shorter period of time, resulting in a less severe load [2]. The stress ratio R gives an indication of how the component is tested, i.e. whether in tension-tension $(0 < R < 1)$, compression-compression $(R > 1)$ or tension-compression $(R < 0)$ loading, with the special case of fully reversed $(R = -1)$ loading [2]. A purely reversing or cyclic stress means when the stress alternates between equal positive and negative peak stresses sinusoidally during each cycle of operation. When a specimen is placed in R = -1 loading conditions at a steady state response around a resonance frequency, two Operating Deflection Shapes (ODS) can be extracted; the shape of the mode shape during a positive and a negative cycle of vibration - later discussed as the crack-opening and crack-closing deflection.

2.4.2 Review on forced vibration response

In real fatigue experiments the Single Degree Of Freedom (SDOF) model still holds. For a fatigue test carried out in a hydraulic tensile machine at R = -1, the case is perfectly represented by the SDOF with the excitation force applied to the mass [2]. The simplest mathematical description of a dynamic system come from the mass-spring-damper system shown in Figure 2.9. This system is called SDOF because its motion can be captured by using only one independent variable, which, in this case, is the vertical motion $y(t)$ of mass m. The equation of motion in this simple case, when an external force $F(t)$ is acting on the mass, is

$$m\ddot{y} + c\dot{y} + ky = F(t) \tag{2.4.3}$$

where m is the mass of the SDOF system, $\dot{y}$ and $\ddot{y}$ are respectively the first and second time derivative of displacement, c is the damping coefficient and k is the stiffness of the spring.

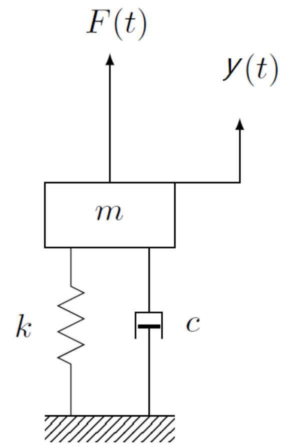

Figure 2.9: SDOF viscously damped system subjected to an external load [2].

When solved, equation 2.4.3 gives a solution of the type,

$$y(t) = Ae^{-\xi\omega_n t}e^{i} \tag{2.4.4}$$

where A is the vibration amplitude at time t = 0, ω_n the resonance frequency, ξ the damping ratio and ω the response frequency, defined as,

$$\omega_n = \sqrt{\frac{k}{m}} \tag{2.4.5}$$

$$\xi = \frac{c}{2\sqrt{km}} \tag{2.4.6}$$

$$\omega_d = \omega_n\sqrt{1-\xi^2} \tag{2.4.7}$$

An important note here is that the stiffness is proportional to the resonance frequency.

If the case that $F(t)$ is harmonic is considered in the equation of motion, it is found most convenient to do so in terms of a complex exponential:

$$F(t) = Fe^{i\omega t} \tag{2.4.8}$$

in this, F denotes the excitation amplitude and ω is the excitation frequency. When solving equation 2.4.3, it gives a complex solution with magnitude and phase, called receptance ($\frac{y}{F}$); a dimensionless FRF in the form of:

$$G(\omega) = \frac{y}{F} = \frac{1}{(k-\omega^2 m) + i(\omega c)} \tag{2.4.9}$$

Since G is a complex number, it is possible to express it as a complex exponential with magnitude $|G|$ and phase ϕ,

$$|G| = \frac{|y|}{|F|} = \frac{1}{\sqrt{(k-\omega^2 m)^2 + (\omega c)^2}} \tag{2.4.10}$$

$$\Phi = \arctan\left(\frac{\omega c}{k-\omega^2 m}\right) \tag{2.4.11}$$

A similar configuration could be achieved by means of an electromagnetic shaker exciting a specimen via base excitation. The lumped parameter model of this system is sketched in

Figure 2.10, and it is described by a viscously damped mass-spring system. The dynamic excitation is given by the displacement of the base as a function of time $y_b(t)$, rather than by a force acting directly on the mass [2].

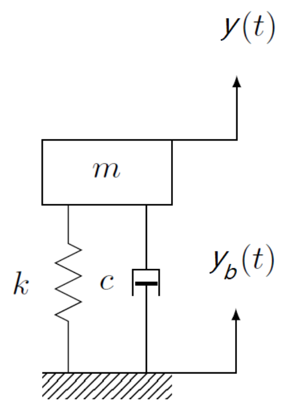

Figure 2.10: SDOF viscously damped system subjected to a harmonic motion of the base[2].

The overall idea is still valid but the phase lag and the transmissibility in a base excitation between the base and mass displacement are given by equations 2.4.12 and 2.4.13.

$$\Phi = \arctan\left(\frac{mc\omega^3}{k(k-\omega^2 m)+(\omega c)^2}\right) \tag{2.4.12}$$

$$|G(\omega))| = \frac{|y|}{|y_b|} = \frac{\sqrt{k^2+(\omega c)^2}}{\sqrt{(k-\omega^2 m)^2+(\omega c)^2}} \tag{2.4.13}$$

In addition, exciting the component around the resonance frequency, the first order Taylor expansion of Equation 2.4.11 can be written as [2]:

$$\phi(k=\omega^2 m) = \arctan\left(\frac{m\omega}{c}\right) + \frac{m^2\omega(k-m\omega^2)}{c^3+cm^2\omega^2} + O\big((k-m\omega^2)^2\big) \tag{2.4.14}$$

Equation 2.4.14 shows that the phase is directly proportional to the stiffness for sufficiently small stiffness variations at constant excitation frequency.

2.5 Vibration fatigue testing for identification of damage initiation in composites

Investigating the crack-growth as a result of vibration loading has been done experimentally and numerically. This project has its roots in the work carried out by Di Maio at the University of Bristol. In his work, Di Maio introduced a method for contactless endurance testing. The research of High Cycle Frequency (HCF) testing continued at the University of Bristol with the work carried out by Magi [2].

2.5.1 Vibration fatigue testing with a plydrop sample

Following a natural evolution and due to the challenges of the contactless method, Magi improved the method and mounted a sample with a plydrop on the shaker for testing at dynamic resonance conditions. A ply-drop is a necessary feature for many components and it is a likely place from which the delamination could initiate; it serves as stress raiser in the material

[2]. He then applied his experimental technique to investigate the fatigue life of Carbon Fibre Reinforced Plastic (CFRP) specimens. The setup can be seen in figure 2.11.

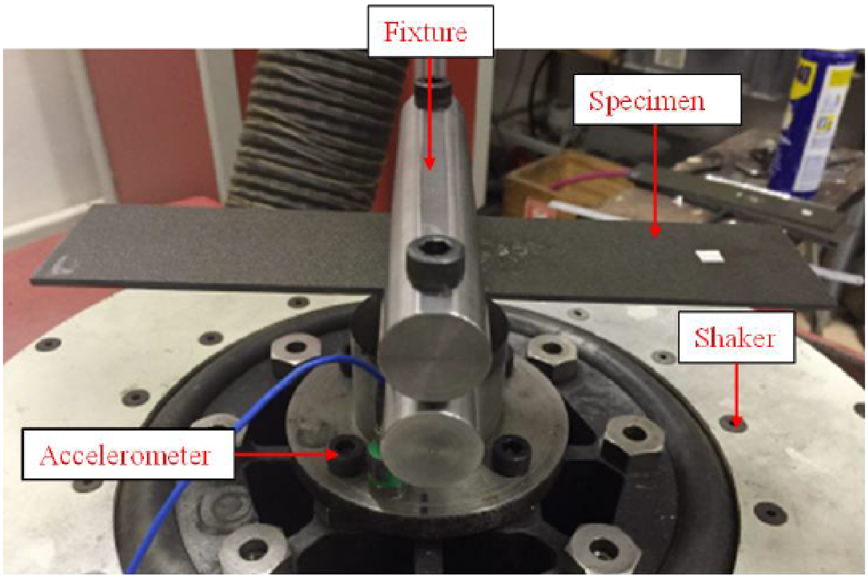

Figure 2.11: Plydrop specimen clamped for testing [12].

Formerly, the testing procedure consisted in exciting a component to its first bending mode, at constant vibration amplitude and constant phase response, in order to maintain the loading frequency at the peak of resonance. Thus, the more the component got damaged, the more the resonant frequency decayed due to a continuous stiffness reduction [2]. Even though, most dynamic tests trace the changes in the resonance frequency by maintaining a constant response phase, Magi implemented a Frequency Lock Loop for his experimental investigation. In fact, he maintained a constant excitation frequency throughout the endurance test while monitoring the dynamic parameters (e.g. the response phase) of the laminates. He reported that by fixing the excitation frequency one can observe how the dynamics of the specimen evolved due to the change of its internal stiffness distribution [12]. Thus, he proposed that the stiffness degradation of testing component can be measured by the change in their dynamic parameters (e.g. response phase / acceleration) during cyclic loading [25]. By monitoring the dynamic parameters, it was clear that, as soon as a delamination initiated, the phase-drops linearly, as seen in figure 2.12. Prior to this failure criterion, there were no indications of the damage evolution.

The breakthrough of this critical event was observed by correlating and analysing all the parameters captured by MONTEVERDI (a software suite, coded in LabVIEW) during the tests. An X-ray CT-scan confirmed that the onset of delamination occurred at the moment when the critical event was captured by the response phase-drop, also seen in figure 2.12. Which is also directly the limitation of investigating this sample; observing the crack by means of a CT-scan is an extensive operation. Measuring the crack is a time-consuming effort.

To prove the feasibility of predicting the critical event has subsequently be done by means of a Finite Element Analysis (FEA). The plydrop model can be seen in figure 2.13.

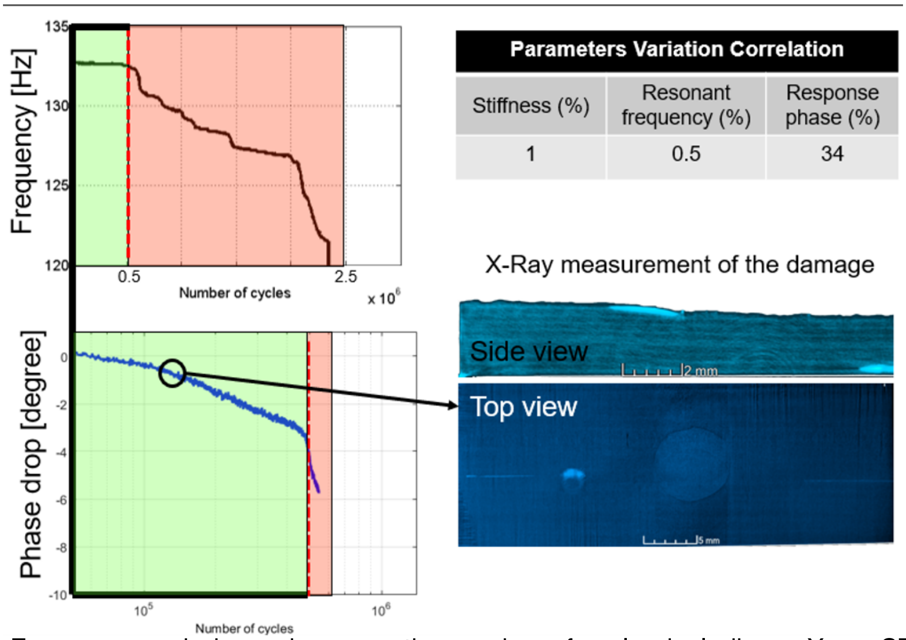

Figure 2.12: Frequency and phase-drop over the number of cycles including a X-ray CT-scan of the plydrop sample.

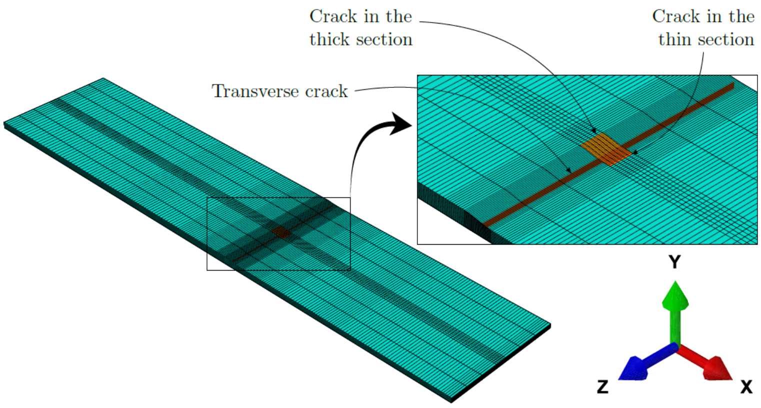

Figure 2.13: FE model with perspective view of the model showing the three types of crack [2]

The occurrence of the critical event has been proven to be driven by the variation of the strain energy release rate, which in turn is a consequence of the geometry of the component. A linear steady state dynamics analysis has been performed to the vibrating structure. The sample is vibrating as a function of an alternating load through the fully reverse cycle of R=-1. It has been demonstrated that the dynamic VCCT has the capability of solving such complex problem with repeated quick linear perturbation analysis, despite having some limitations. Linear analysis cannot take into account true contact, thus it is challenging to simulate effects of friction between delaminated plies and to accurately predict the mode mixity (the influence of $\mathrm{G_I}$ and $\mathrm{G_{II}}$ to the crack opening) and the stress ratio at the tip of the crack [2].

Following di Maio and Magi's footsteps, Voudouris [12] examined the fatigue life of composite laminates under vibration fatigue loading and elevated ambient temperature conditions both experimentally and numerically [12]. His study is aiming to express the relation between the mechanical and thermal responses of a CFRP specimen that undergoes resonance testing. Voudouris, first and foremost, developed an experimental technique for the investigation of vibration fatigue of composites, at different exposure temperatures; exploiting the failure criterion

[12] that had already been introduced for resonance testing by Di Maio and Magi [2].

Finally, yet importantly, Voudouris' numerical investigation revealed how the delaminated area will behave during vibration testing and what mechanisms can drive the damage propagation. He simulated the mechanical response of the composite laminates that was observed during the experimental investigation. With reference to figure 2.14, one can observe that both the self–generated temperature and the response phase can be separated into 3 distinct regions. In fact, one can observe the fatigue life can be divided into 3 quasi-linear trends [12].

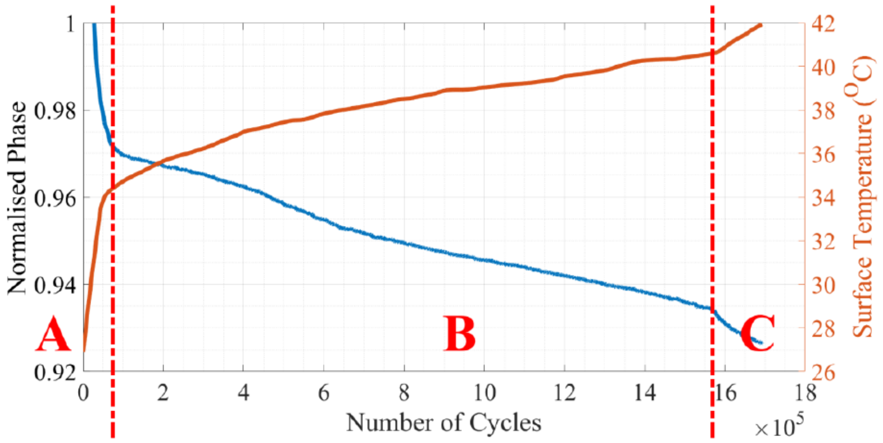

Figure 2.14: The three distinct regions of the phase and self – heating temperature evolutions [12].

For this reason, it was decided that interrupted tests will be conducted in an effort to analyse the fatigue damage development during endurance testing as well as to understand the difference between the 3 stages. The experiments were interrupted at about every 2.5×10^5 cycles [12]. Finally, to demonstrate the feasibility of the FE models, correlating the experimental and the numerical results. As in particular, experimental parameters (e.g. crack growth rate, frictional heat) are principally challenging to extract during resonance testing. The Virtual Crack Closure Technique (VCCT) results, with which one is able to calculate the $\mathrm{G_I}$ and $\mathrm{G_{II}}$ numerically, seemed to follow closely the experimental behaviour. In fact, it was presented that the simulated critical event at elevated temperatures, follows an identical behaviour to the experimental observations [12]. However, the crack length is difficult to obtain from this sample, therefore a new sample has been established.

2.5.2 Vibration fatigue testing with a cut-ply sample

After di Maio, Magi and Voudouris, the project continuous under the name HEGEL in collaboration with TWI and NLR as a consortium. The main objective was to develop a new method to characterize the fracture mechanics properties testing a composite specimen with a new application stacking sequence. With this new sample the HEGEL project tries to overtake time consuming ASTM standard test and the time-consuming X-ray CT scanning of the samples. The new CFRP coupon did not make use of a plydrop, but used a cut-ply; a pre-installed transverse crack located 10 mm from the clamping, as seen in figures 2.15 and 2.16. The new sample has the following layup: [90/0cut/90cut/0/90/90/0/90/0/90]. With use of the new sample it is possible to measure the crack tip with use of microscopic images instead of X-ray CT scans.

Figure 2.15: Crack path predefind direction [7].

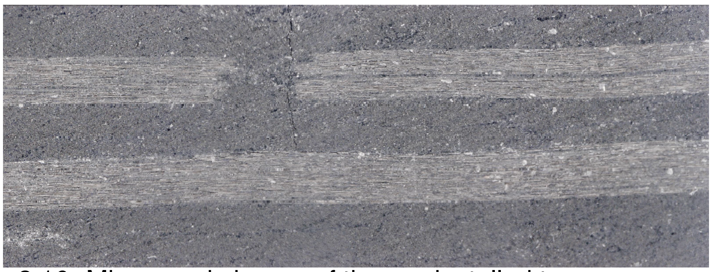

Figure 2.16: Microscopic image of the pre-installed transverse crack [7].

The sample is tested similar to the plydrop specimen, and again the phase-drop serves to be a reliable and sensitive parameter. During the experiments, the results show that stiffness degradation, resonance decay and phase-drop have a strong relationship, thus one can analyse the structural degradation phenomenon following different parameters such as the magnitude and slope. A linear slope shows that phase decays with the same degradation during fatigue life. This can be seen in figure 2.17.

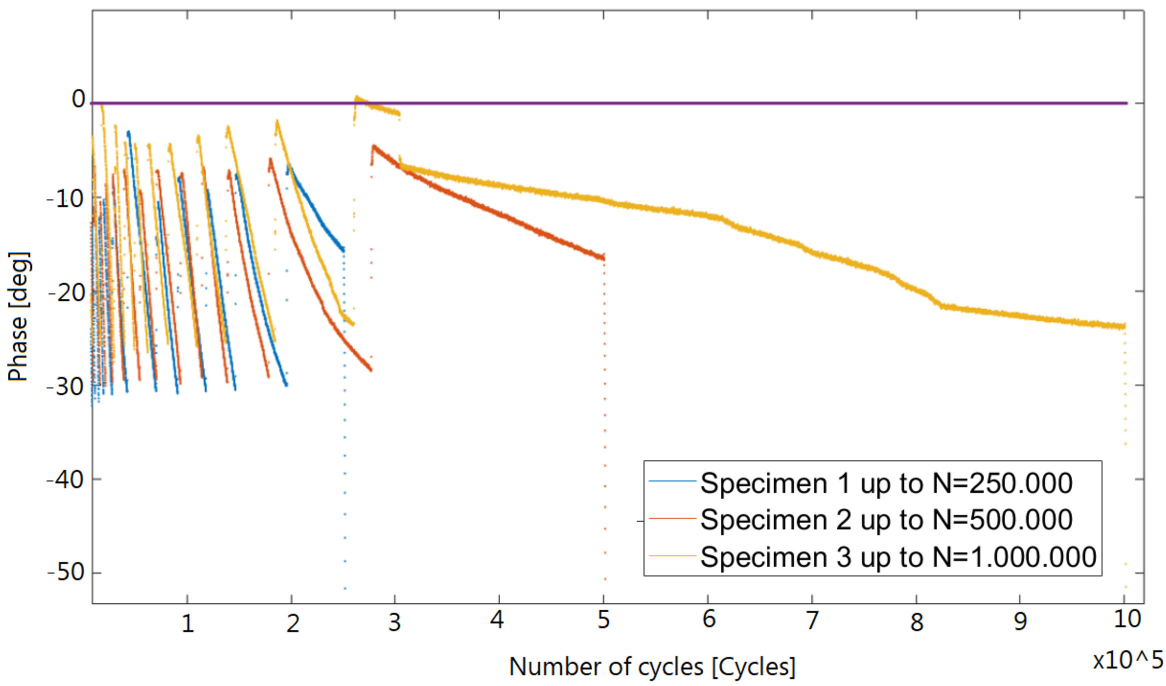

Figure 2.17: Experimental measurements of phase-drop over cycles for 3 specimen [7].

Moreover, an interesting crack growth investigation has been performed, measuring the length after different vibration fatigue tests, and one can observe the propagation rate of a T-shape crack which is also affected by the proximity of the clamping side, as seen in figure 2.18. Here it can be seen that over 1.000.000 cycles, the crack grows more to the clamping side than towards the direction away from the clamping side.

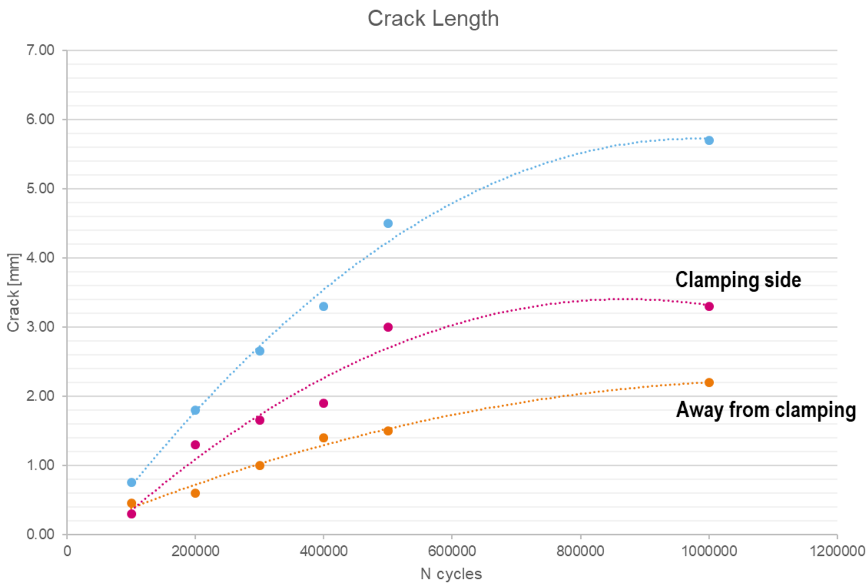

Figure 2.18: Microscope measurements of crack lenghts versus the number of cycles for blue) the total crack length red) the crack length of the crack closest to the clamped side and orange) the crack length of the side away from the clamped side[7].

A new numerical model has been established for this new cut-ply sample. Where the crack growth is calculatd again by means of the VCCT analysis. Here, the VCCT is performed outside ABAQUS; the $\mathrm{G_I}$ and $\mathrm{G_{II}}$ values are calculated in MATLAB. In the numerical model, an interface between cut-plies and bottom plies is made with use of spring elements that connect two points in order to have the possibility to open a crack by eliminating the spring connection. Thus, the nodes of the elements of different instances are duplicated at the interfaces, and a massless spring is applied between each of them for every crack opening mode, as seen in figure 2.19 [7].

Figure 2.19: Finite element model on ABAQUS with springs interaction (purple dots) and the non-structural mass on the clamping position (green zone) [7].

To simulate the crack-opening, the MATLAB script changes the definition of the spring elements, removing a number of node pairs. In this way, the crack propagates. The work helps with the characterization of mechanical property of CFRP specimens through the crack growth rate investigation and SERR calculation. However, this again is a linear analysis, which cannot take into account true contact [2]. Thus, this framework, carried out with an experimental and FEA hybrid method, can find mechanical parameters involved in fracture mechanics. Finally, this analysis lead to the Paris'law parameters by a correlation between experimental and numerical output data.

2.6 Virtual Crack Closure Technique

Originally proposed by Rybicki and Kenninen, the Virtual Crack Closure Technique is based on the Linear Elastic Fracture Mechanics (LEFM) and Irwin's criterion [26]. The VCCT is used in FE analysis to calculate the SERR at the crack tip based on the idea that the energy released to open a crack is equal to the work the forces at the crack tip have to do to close the same crack. When the SERR is higher than the fracture toughness of material, those nodes are untied and the crack is open, otherwise they remain bonded together [7]. With a reference to figure 2.20, the work required for the crack closure is defined as following for the 2D case:

$$\Delta E = \frac{1}{2}[X_{1l}\Delta u_{2l} + Z_{1l}\Delta w_{2l}] \tag{2.6.1}$$

where X_{1l} and Z_{1l} are the horizontal and vertical forces at the node l when the crack is closed and Δu_{2l} and Δw_{2l} are the horizontal and vertical displacements in l when the crack is open.

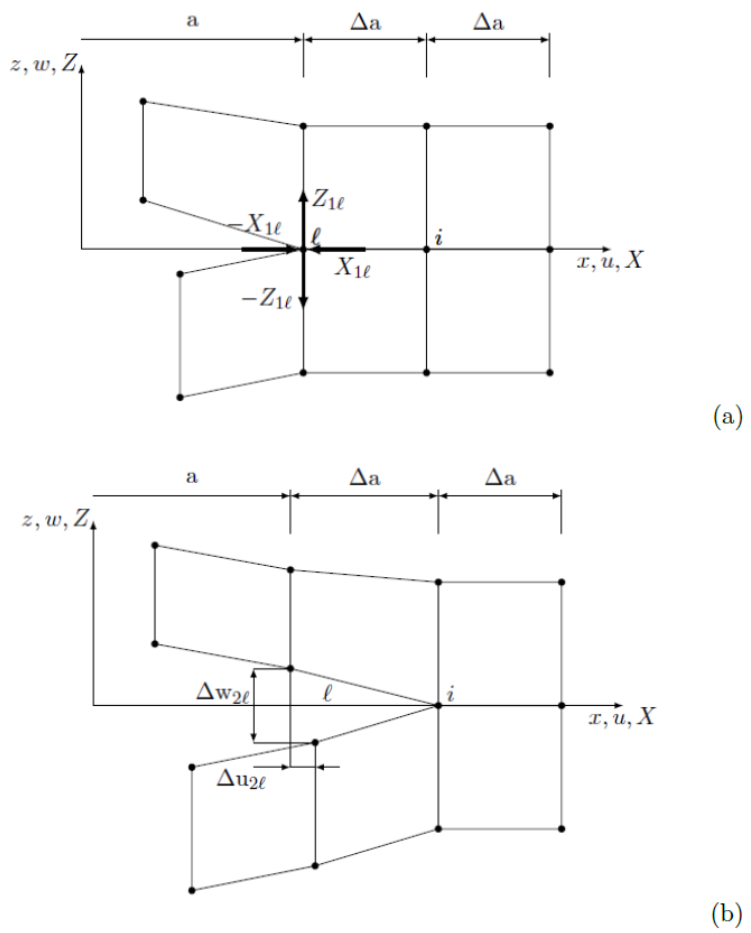

Figure 2.20: Two steps crack closure method: (a) the crack is closed by forces at nodes and (b) the crack is open and the nodes are untied. The SERR is equal to the work the forces in the first step do to move the nodes up to the points of the second step [7].

Another assumption is added to the conservation of energy: in the first approximation, the state at the crack tip is not changed by the crack propagation of Δa. This assumption simplifies the entire formulation, allowing to calculate the SERR in one singe step without a feedback loop, as seen in figure 2.21.

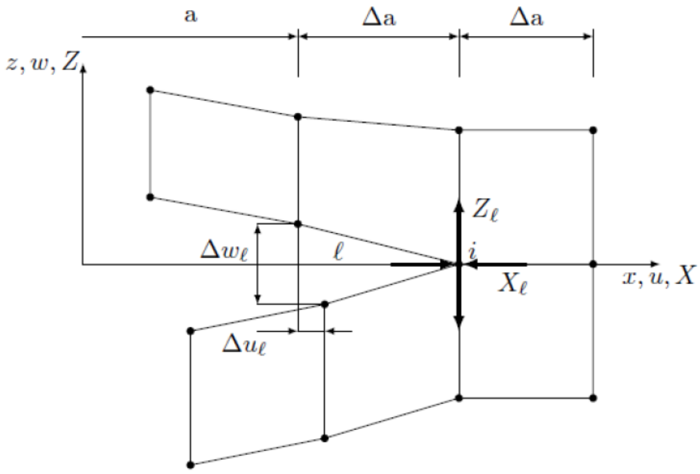

Figure 2.21: Single steps (virtual) crack closure method. The SERR is equal to the work the forces in i do for the displacement of the node l [7].

The delamination in the 2D model may grow under a combination of mode I, tension or peel and mode II, in-plane shear. It could be extended with mode III transverse shear, but this is neglected in this research as there is only in-plane deformation. The value of G_T can be achieved for linear analyses by using the $\mathrm{G_I}$ and $\mathrm{G_{II}}$. [27]. This research will solely look into the mode I and mode II separation, mode III is excluded as it is an 2D model. The equations are given in constitutive relations equations,

$$G_I = \lim_{\Delta a \to 0} \frac{1}{2b\Delta a} Z_i(\Delta w_l) \tag{2.6.2}$$

$$G_{II} = \lim_{\Delta a \to 0} \frac{1}{2b\Delta a} X_i(\Delta u_l) \tag{2.6.3}$$

In general, the smaller the distance between neighbouring nodes, Δa, the more accurate equations 2.6.2 and 2.6.3 will predict the strain energy release rate values. Where b is the thickness of the specimen.

The VCCT method simulates crack propagation and delamination by applying constraints to the nodes on the crack path. The nodes in front of the crack tip are coupled, to be released after the fracture criteria is met, simulating the advance of the crack [26], as shown in figure 2.20. The VCCT requires a pre-defined crack path, which is restricted to the element boundaries [31]. As the model is governed by LEFM, before damage occurs, the system is linear-elastic. After the fracture criterion is reached, the constrained nodes become separated immediately without a damage evolution. The most common fracture criterion used in VCCT analyses is the BK-Law [32]. This criterion is based on the total energy release rate (G_T) and it is accomplished after the critical value (G_T^C) is reached [26] :

$$f = \frac{G_T}{G_T^C} \tag{2.6.4}$$

The crack-tip node debonds when the fracture criterion reaches the value of 1.0. Here, the calculated SERR is larger than the critical SERR value. Where,

$$G_T = G_I + G_{II} \tag{2.6.5}$$

$$G_T^C = G_I^C + \left(G_{II}^C - G_I^C\right)\left(\frac{G_{II}^C}{G_I + G_{II}}\right)^{\eta} \tag{2.6.6}$$

here η is the BK law parameter, which is 1.45 in accordance with previous literature. [7] The critical energy release rate values are material depending properties.

Chapter 3

Remastered Finite Element Model

A new FEM-based model, capable of predicting fatigue crack growth, focused on delamination cracks, is developed with use of ABAQUS. The model is a remastered version of the cut-ply sample from the HEGEL project. Where contact elements are included in the delamination area and a small initial delamination length of 0.1 mm is being used.

Within this model, the analysis is carried out in two ways: First, the FEM model identifies the dynamic nature by means of a Steady State Dynamic analysis. The dynamics is broken down into a stepped static solutions for steady-state vibration response. The steady-state solutions will create a time-step at which the static analysis is performed. Second, the crack propagation caused by vibration fatigue is considered in a static environment, based on Virtual Crack Closure Technique (VCCT). In this static envionment, the contact is established to include interlaminar frictional effects. The two analyses share the same part, assembly and material properties, but use different loads, boundary conditions and interaction settings. The detailed description on how to model this FE model can be seen in Appendix A.

The procedure to develop the FEM modelling approach, with both the static environment and dynamic environment, will be highlighted in more detail in the next chapter. Globally, the roadmap to achieve the crack growth is visualized in figure 3.1. Here the green steps are the functionalities to be realized by the dynamic environment and the blue steps are the functionalities to be developed by the static environment.

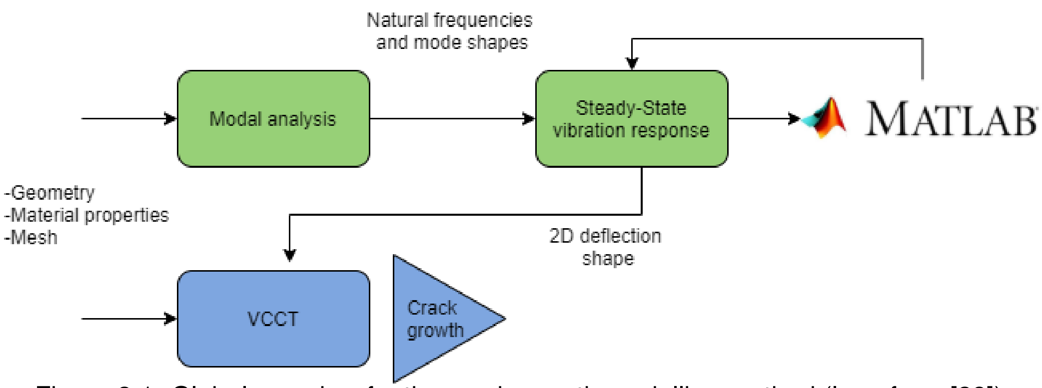

Figure 3.1: Global overview for the crack-growth modelling method (logo from [28]).

Both environments have the same input parameters of the geometry, material properties and mesh properties. When the SSD response is calculated, an iterative displacement solver in

MATLAB is responsible for maintaining displacement control. Then, the deflection shape of the SSD model serves as an input as a boundary condition for the static environment. From here, the VCCT can be performed to calculate the G_I and G_{II} , from which the crack growth is established. The reason for performing this vibration-driven modelling approach is explained in more detail in appendix B.

3.1 Geometry

The total specimen modelled is a 260mm long and 25mm wide laminate. Each laminate consists of 10 unidirectional laminae of 0.14mm thickness. The overall thickness of the laminate is therefore 1.4mm. The lay-up sequence of the laminate is

$$[90° - cut/0° - cut/90° - cut/0°/90°/90°/0°/90°/0°/90°]$$

The crack is located 10 mm from the clamped region in the right halve of the specimen. The crack is modelled as a gap of 2mm. The onset of the crack is predefined and it is thus known a priori where the delamination will grow. In order to replicate the transverse crack across the first three plies from the top, the overall model consisted of three parts, as seen in figure 3.2: bottom part, top left part and top right part. In here, the reference node is highlighted as well. At this node, the displacement is captured. In the experimental setup from Peluzzo [7], this point was also taken to measure the vibration response by means of a single point Laser Doppler Vibrometer (LDV). Michel used the LDV to capture the operating deflection shapes in real life [7]. Therefore, this point is also taken as a reference for the numerical vibration response. The technical drawings of the parts can be obtained in Appendix C.

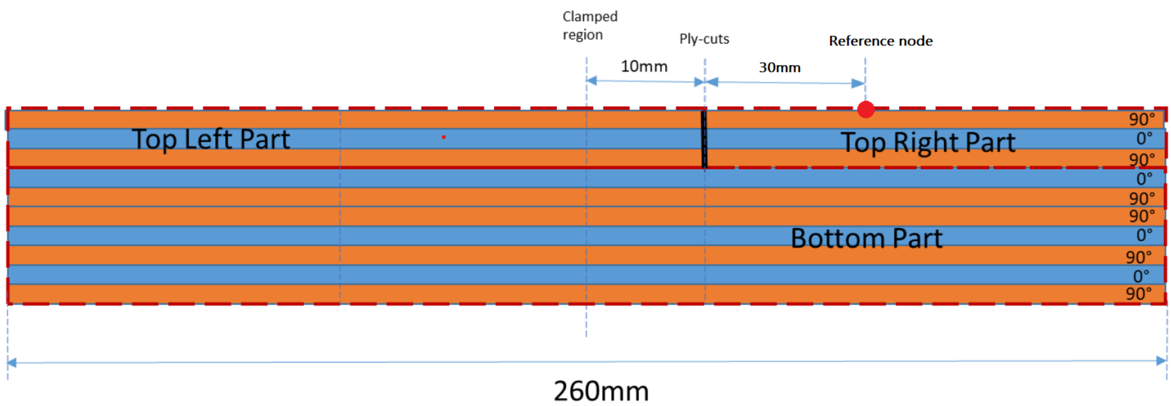

Figure 3.2: Schematic overview of the specimen geometry used in the FE models.

3.2 Material Properties

The material properties of the thermoset material will be assigned to the model according to the lay-up sequence. These properties are summarized in table 3.2.1.

standard modulus carbon thermoset		Dry specimen at RT
Consolidated ply thickness [mm]		0.14
Mass density [tonne/mm3]		1.59e-9
Young's modulus 0^o [MPa]	E_1	124250
Young's modulus 90^o [MPa]	E_2	7660
	$E_2 = E_3$	7660
In-plane shear modulus $\pm 45^o$ [MPa]	G_{12}	4348
	$G_{13} = G_{12}$	4348
	G_{23}	1450
Poisson ratio $\pm 45^o$ [-]	ν_{12}	0.36
	ν_{23}	0.5
	$\nu_{13} = \nu_{12}$	0.36
Tensile strength 0^o [MPa]	σ_{11}	2410
Tensile strength 90^o [MPa]	σ_{22}	86
In-plane shear strength $\pm 45^o$ [MPa]	σ_{12}	152
Compressive strength 0 ^{o} [MPa]	σ_{11}	1300
Mode I interlaminar Fracture Toughness [mJ/mm^2]	G_{IC}	0.349
Mode II interlaminar Fracture Toughness [mJ/mm^2]	G_{IIC}	0.806
Mode III interlaminar Fracture Toughness [mJ/mm^2]	G_{IIIC}	0
Friction coefficient [-]	μ	0.1
Damping constant [Ns/m]	c	0.01

Table 3.2.1: Summary material parameters of the thermoset composite [7] [29].

3.3 Mesh

In order to carry out the FEA, an element type needs to be chosen. As for all the previous numerical models out of the literature, 8-node quadrilateral continuum solid shell elements were used. However, these were used for a 2.5D model. The current model is a 2D model, therefore, a change in elements has been made towards CSP8R elements.

Chosing the CSP8R elements (An 8-node biquadratic plane stress quadrilateral with reduced integration), a shearlocking issue has been overcome. However this increased the computational effort significantally. Therefore the amount of nodes has been reduced to 4 instead of 8, increasing the numerical error, but making it workable for the time-span of the research. This results in an element choice towards CPS4R, the 4-node plane stress element with reduced integration.

Each ply is characterised by a mesh with a 500 micrometer element size along the length of the specimen and one element through the width. In order to observe small crack growht lengths, a local refinement of 100 micrometer has been applied 30 mm to the right and 30 mm to the left of the crack. This results in a total number of nodes of 11936 which are connected by 9940 elements of type CPS4R.

Finally, the plies at the interfaces have spatial matching nodes. This is a requirement when defining VCCT interaction surfaces-to-surface interactions, used to replicate the delamination occurring between the 3rd ply and the 4th ply.

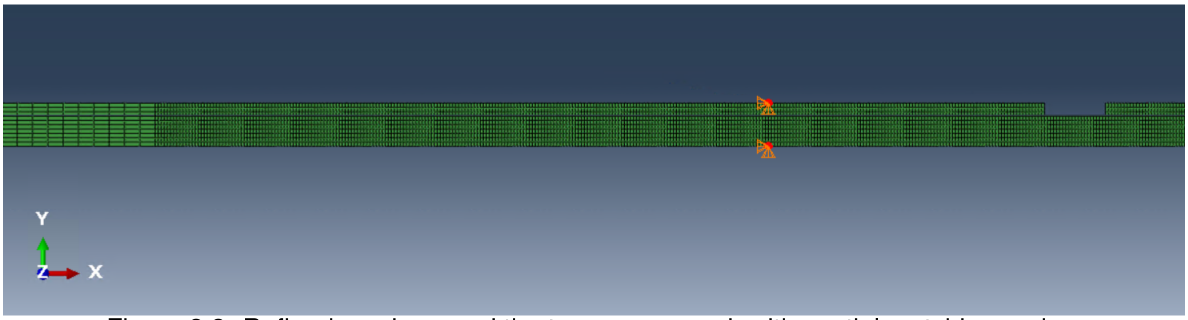

Figure 3.3: Refined mesh around the transverse crack with spatial matching nodes.

3.4 Loads, Boundary conditions & Interactions

In this section, the appliance of the load, boundary conditions and the interactions are described for both the dynamic as well as the static environment.

3.4.1 Dynamic environment

The dynamic load is applied to the nodes at the outer edges of the composite structure. The schematic of the structure can be obtained in figure 3.4. The boundary conditions are exact in the middle of the plies, where it has a point constraint on the top and on the bottom of the structure, suppressing the U_1 in and U_2 direction. The rotation around the z axis is remained free.

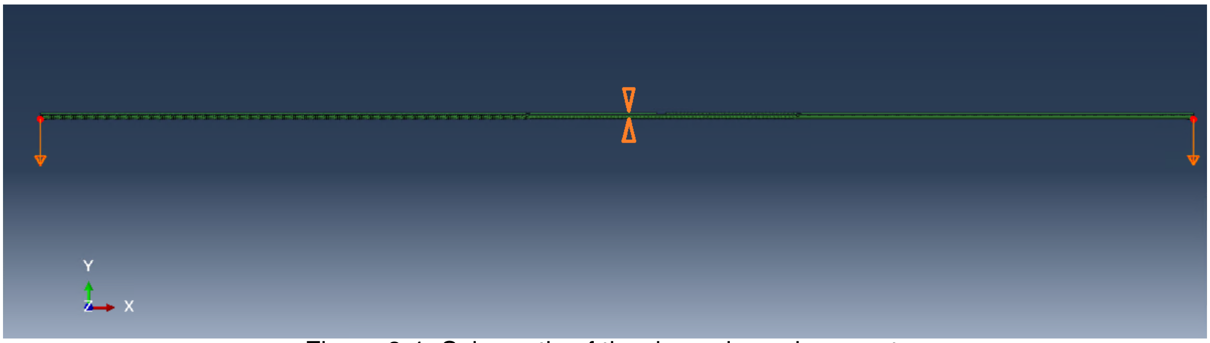

Figure 3.4: Schematic of the dynamic environment.

The three parts, as mentioned in section 3.1 needs a form of assembly, to keep the parts from expanding in space when the simulation is run. Therefore, the two top parts are connected to the bottom part by means of a tie constraint. A tie constraint ties two separate surfaces together so that there is no relative motion between them. The tie constraint is the constraint between the top surface of the bottom part, which connects to the node set of the top parts: 'The bonded node set'. With the bonded node set, it is possible to manually coordinate the cracklengths. As the mesh has a element width of 100 micrometer, opening each additional node results in a increased cracklenght of 0.1 mm.

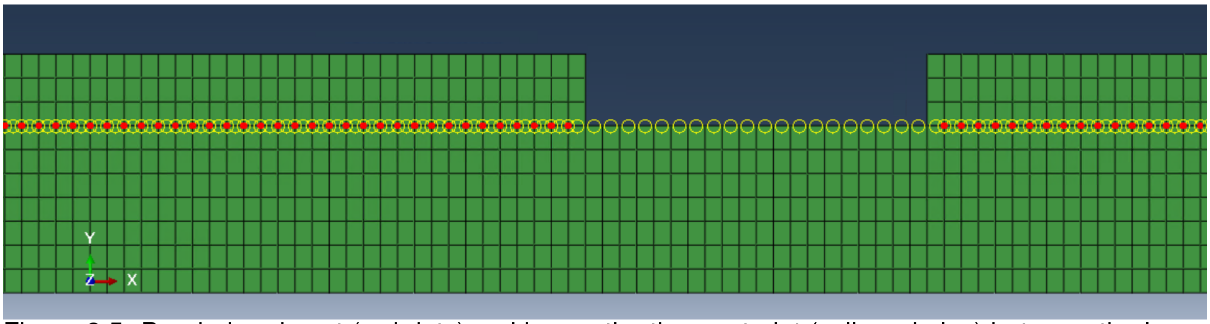

Figure 3.5: Bonded node set (red dots) making up the tie constraint (yellow circles) between the lower and top parts.

3.4.2 Static environment

The load and boundary conditions in the static model are differently defined than in the SSD model. The deflection of the SSD model serves as an input for the boundary condition of the static model. Therefore, no external load is added to the system. When the SSD model is deformed, the distributed nodal displacement vector is extracted. This displacement field is the boundary condition for the static model.

The interaction between the lower parts and the top part is set up to calculate the strain energy release rate in the crack tips. This can be done with the Virtual Crack Closure Method (VCCT). To apply the VCCT in the model, first a surface-to-surface contact interaction is created, that models the potential crack surfaces using master and slave contact surfaces. The master surface is the largest surface, thus the top surface of the lower part. The slave surface is the smallest, thus the bottom surfaces of the top parts. The two surfaces are initially bonded with a new bonded node set. This bonded node set, however, is different than the bonded node set from the dynamic environment. In the static environment, the bonded node set is left unchanged during the node openings, as the VCCT happens automatically. The bonded node set of the static environment is always defined to have one node opened in the left crack tip and one node opened at the right crack tip. When the distributed nodal displacement field is applied as boundary condition, the crack continues to propagate along the interface between the master and slave surfaces. During the convergence, the static bonded node set opens automatically until it reaches the point where the bonded node set of the dynamic environment is predefined. As this is set as a boundary condition, the crack can not propagate after the bonded node set of the dynamic environment. The convergence step is defined in maximum 10.000 increments with a initial step size of 1e-6, a minimum size of 1e-20 and a maximum size of 0.01.

Chapter 4

Crack-growth modelling procedure

Now the modelling has been explained in detail in the previous chapter, the method for the main objectives is proposed. The method to identify how the crack-growth propagates will be elaborated. In this chapter, the first research objective is investigated. The first objective will primarily develop a framework to investigate the forces at the crack tip acting at two ends of the delamination. It will show how an experimental test can be broken down by finite element analysis to allow such investigation and replace the test.

A hybrid procedure to model the crackgrowth, which is partly automated by an algorithm between MATLAB and ABAQUS and partly manually constructed, will be elaborated. The procedure consists iteratively of the following items as seen in figure 4.1:

1. Construct an initial model where the initial force is large enough to enable crack-growth;
2. Calculate natural frequency and mode shape and perform the Steady State analysis;
3. Run the displacement control algorithm;
4. Transfer distributed nodal displacement from dynamic to static environment;
5. Perform the VCCT analysis to calculate the SERR
6. Analyse the SERR and compare it to the critical SERR;
7. Release more nodes in the dynamic bonded node set to replicate a crack growth and follow the steps from step 2 again.

This procedure is both done for the crack-opening as well as for the crack-closing deflection. The blue steps are performed in ABAQUS, the orange in MATLAB and the yellow outside of these programs in Notepad++ and Excel. The detailed process can be seen on the next page, in figure 4.1. In this chapter, all the individual steps of the crack modelling procedure will be discussed and highlighted. All the modelling steps of these can be seen in Appendix D.

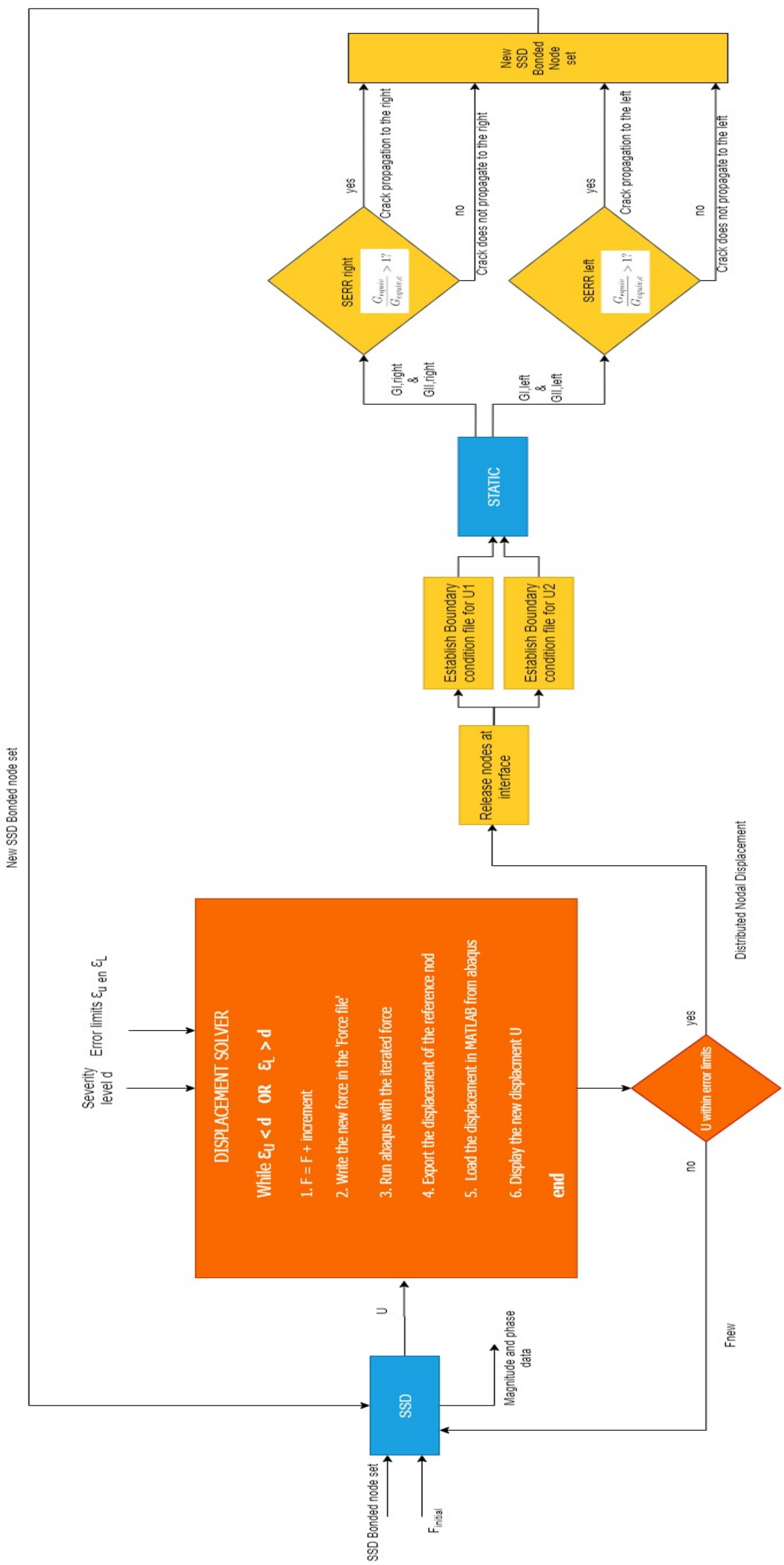

Figure 4.1: Detailed overview of the crack-growth modelling procedure.

4.1 Initial model

The process starts with finding a force large enough to enable crack growth. A certain displacement of the reference node is associated with this initial force. The displacement is also known as the severity level of the system. The process is performed for one severity level; the low severity level. This severity level is found by iterating the initial force, send it through the crack modelling framework and find out whether the force is large enough to generate crack growth. Here the initial crack is modelled by opening the bonded node set one node on both sides. Then the displacement of the reference node at this severity level serves as a reference displacement for the displacement algorithm, to maintain displacement control to the reference displacement.

4.2 Modal- and Steady State analysis

In this section, first the frequency analysis or modal analysis and later the SSD analysis is discussed.

4.2.1 Modal Analysis

The eigenfrequencies are established in the frequency analysis. Here ABAQUS performs eigenvalue extraction to calculate the natural frequencies and the corresponding mode shapes of a system. The first 3 eigenmodes are extracted and are shown in figure 4.2. Due to the introduced crack, the first two eigenfrequencies are close to each other. The first bending mode splits in two shapes in case of the presence of the delamination. However, both indicate the same first bending shape. The only difference is that the first eigenmode is a rocking mode and the second eigenmode a scissoring mode. These rocking mode shapes are never to be seen during the experiments, therefore the calculations are done around the second eigenmode, with the scissoring mode.

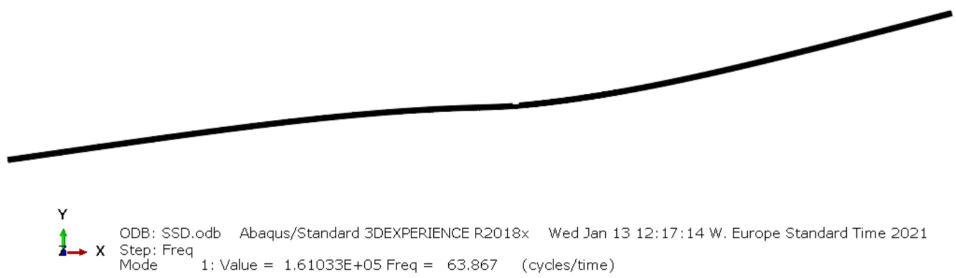

(a) First eigenmode at 63.9 Hz.

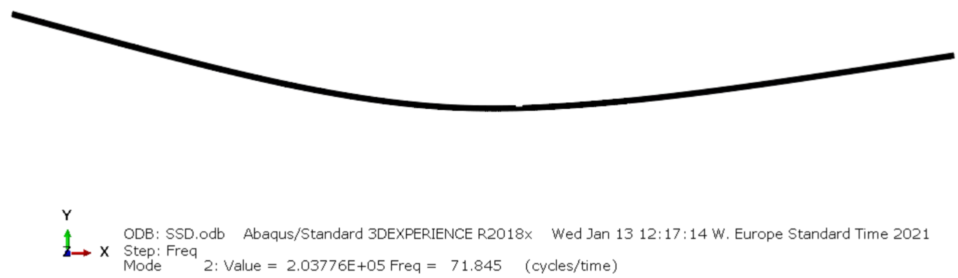

(b) Second eigenmode at 71.8 Hz.

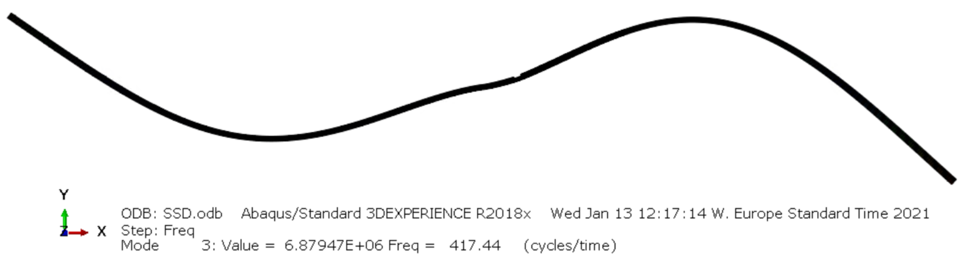

(c) Third eigenmode at 417.4 Hz.

Figure 4.2: Eigenmodes of the (a) First eigenfrequency at 63.9 Hz, (b) Second eigenfrequency at 71.8 Hz and (c) Third eigenfrequency at 417.4 Hz.

4.2.2 Steady State Dynamics analysis

The SSD analysis provides the steady-state amplitude and phase of the response of a system due to harmonic excitation at a given frequency. Such an analysis is done as a frequency sweep by applying the loading at a series of different frequencies and recording the response [24]. In a direct-solution steady-state analysis the steady-state harmonic response is calculated directly in terms of the physical degrees of freedom of the model using the mass, damping, and stiffness matrices of the system. The SSD can be analyzed by either the imaginary and real part of the displacment or by the magnitude and phase plots. In this section, the real and imaginary part of the displacement will be introduced. With use of the characteristics of the real part of the displacement, a pragmatic solution will be proposed to find the outer bending shapes of the fully reverse cycle.

A frequency sweep can be obtained in figure 4.3. In the graph of the real part of the reference displacement, it is evident to indicate the 3 modes as discussed in the section above. The graphs follow the 'reference node', from figure 3.2.

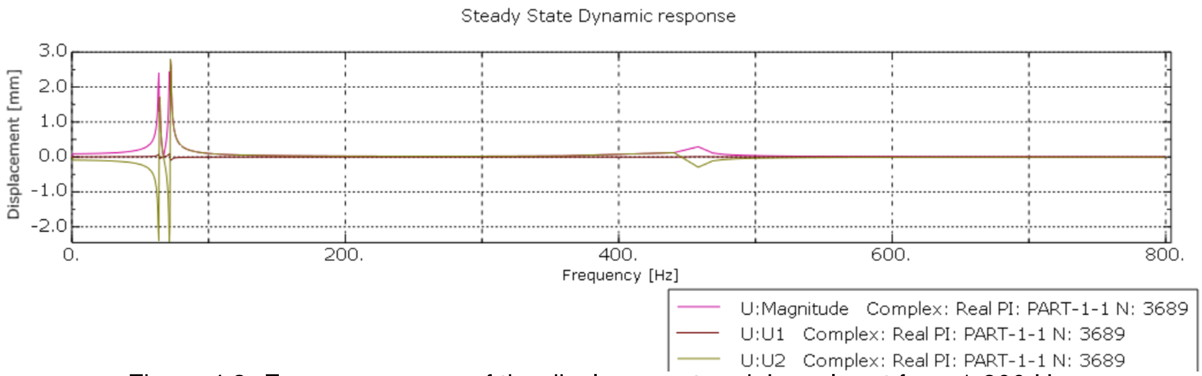

Figure 4.3: Frequency range of the displacement node's real part from 1-800 Hz.

The frequency range of the second eigenmode, representing the scissoring mode, is highlighted in greater detail in figure 4.4. In here, the contribution of both the real part and the imaginary part is shown to the total displacement of the reference node.

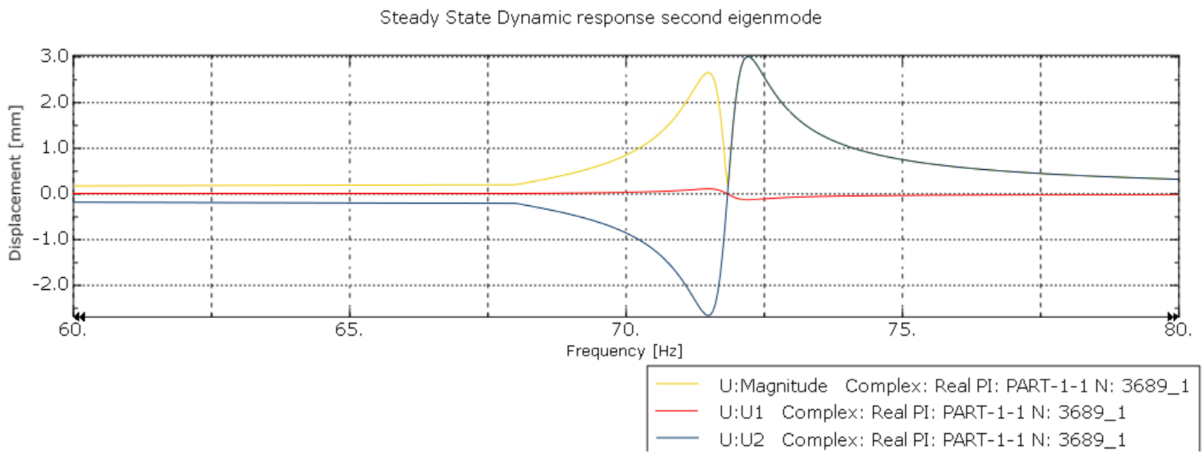

(a) Frequency range of the displacement node's real part around the second eigenmode.

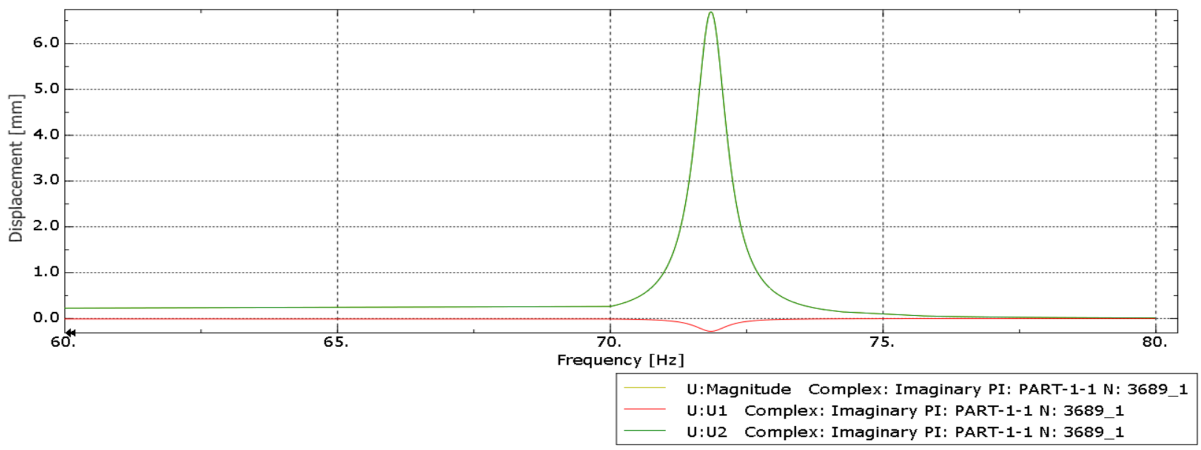

(b) Frequency range of the displacement node's imaginary part around the second eigenmode.

Figure 4.4: Frequency range around the second eigenmode of the displacement node's a) real part and b) imaginary part.

When the model vibrates through the fully reverse cycle, the model vibrates through an outer positive and a negative shape. The two shapes, or Operating Deflection Shapes (ODS) can be categorized as a 'positive-shaped' and 'negative-shaped' deflection. These represent respectively the crack-opening and crack-closing deflections.

In order to obtain these shapes, the following pragmatic solution is proposed: from the real part of figure 4.4a it can be seen that for frequencies slightly above the resonance frequency of 71.8 Hz have a positive displacement and frequencies slightly lower than the resonance frequency have negative displacement. Therefore, the real part of the displacement can be used to construct the positive and negative shape. Note that this should be one and only one frequency; the resonance frequency. The resonance frequency should be the excitation frequency.

For simplification purposes, only the influence of the real part of the displacement is used in the calculations. The imaginary part of the displacement is neglected. A limitation to this pragmatic approach is that the imaginary contribution is not taken into account. This assumption results thus in a displacement which is not the actual maximum displacement. In reality, a combination of the real and imaginary displacement will lead to the magnitude of the displacement.

The ODS', according to a respectively slightly lower and slightly higher frequency than the resonance frequency, are plotted in figures 4.5a and 4.5b

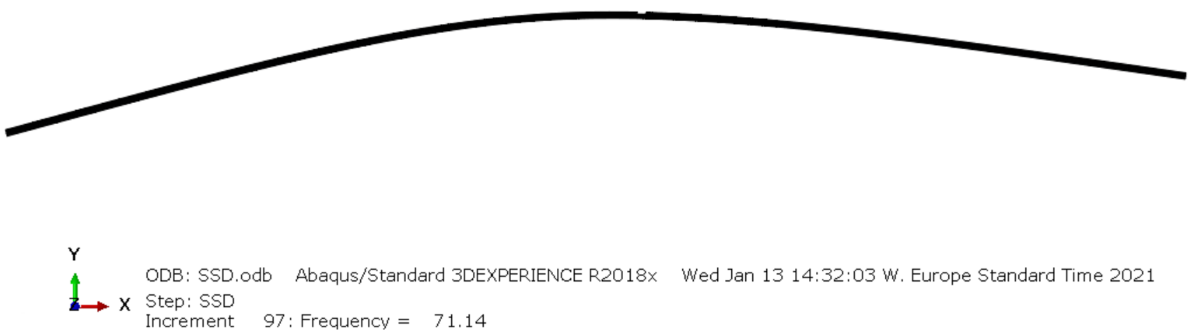

(a) Crack-opening deflection.

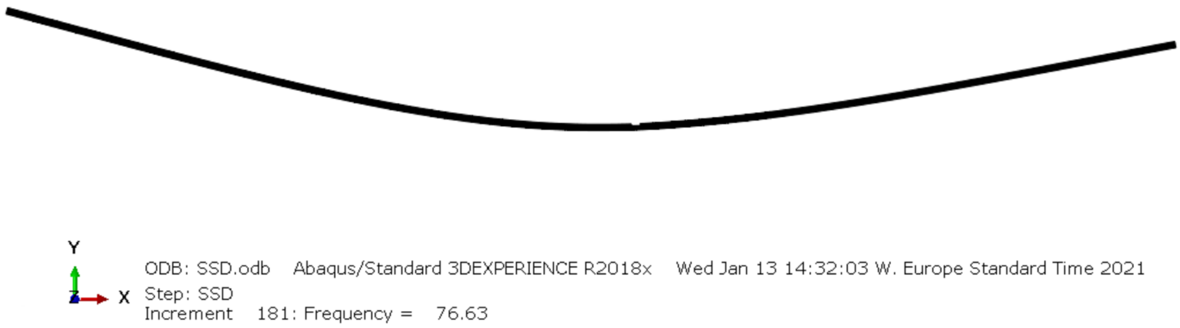

(b) Crack-closing deflection.

Figure 4.5: Mode shapes of (a) Slightly lower frequent than the resonance frequency: 'crack-opening deflection'(b) Slightly higher frequent than the resonance frequency: 'crack-closing deflection'.

These ODS' also follows from an analysis of the phase plot, as seen in figure 4.6. The phase is more associated with this research, as it provides information about the phasedrop. The real and imaginary part of the displacement are related to the phase according to,

$$\phi = \arctan\left(\frac{U_i}{U_r}\right) \tag{4.2.1}$$

where U_r and U_i are respectively the real and imaginary part of the displacement. The phase plot provides useful information, as the phase-drop will be a highly-sensitive parameter for identifying crack-growth. Exactly at the resonance frequency of 71.8 Hz, the phase angle equals 90. When a frequency is obtained lower than the eigenfrequency, resulting in $\phi < 90$, the right-hand-side of the equation becomes positive, resulting in a positive deflection. In contrary, a frequency higher than the resonance frequent, resulting in $\phi > 90$, gives a negative expression, resulting in a negative deflection.

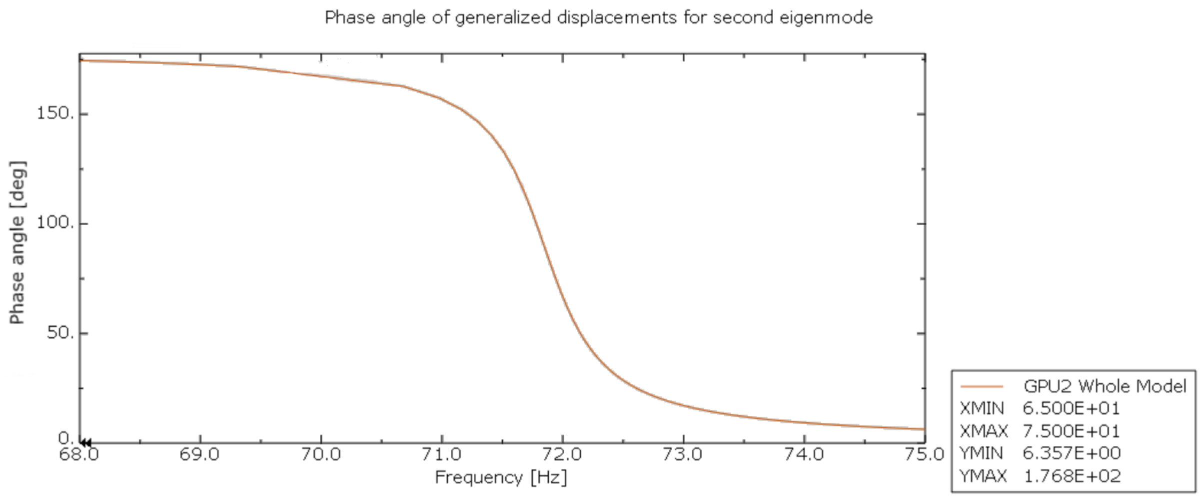

Figure 4.6: Phase angle of generalized displacement for the second eigen mode.

The entire crack-modelling procedure of figure 4.1 is performed for each of the two deflection shapes; for the crack-opening and crack-closing deflection.

The SSD environment will be run firstly with the initial dynamic bonded node set. This is the bonded node set where one node is opened for both the left crack and on right crack. This is the initial crack length. This bonded-node set will be updated after running through the entire crack-modelling procedure; that is, after each iteration. The first iteration of the crack-modeling procedure is done with an initial force from section 4.1. The SSD analysis will thus be run firstly with an initial bonded node set and an initial force.

The displacement of the reference node follows from the initial SSD analysis. This is the displacement which will be used as a reference for the displacement control. The entire deflection shape will thus be converged to this particular reference displacement of $\pm$ 0.945mm: it converges to +0.945mm for the crack-closing deflection and -0.945mm for the crack-opening deflection.

The function of the displacement solver is to maintain the steady state displacement control of the reference node during crack propagation. As the crack opens and the crack propagates, the stiffness of the ply decreases. This will result in the entire phase and magnitude graphs shifting to the left as the resonance frequency is also directly affected by the stiffnessdrop; the resonance frequency decreases. When the force is not adjusted accordingly, the ply will vibrate with an increased amplitude. This is called the force controlled. However, as in the experiments, it is practically more desired to cope with displacement control. Thus the force should be adjusted to maintain a constant displacement for a decreasing stiffness based on the reference nod displacement.

The displacement solver is an algorithm which links MATLAB with ABAQUS in an iterative loop. The solver in MATLAB starts with an initial force. The force is written in a ‘Force file’. This new ‘Force file’ is loaded in the SSD input file (.inp) and is send to ABAQUS where it runs the Steady State analysis. The output is the displacement of the reference node, which is exported in a data (.dat) file. The displacement is then imported in MATLAB and compared to the reference displacement with a certain error margin of $\pm 1\%$: the solution space.

When the error criterion is not met, the solver adds or subtracts a small increment to the force and overwrites the 'Force file', until the displacement will converge to a solution within the solution space.

The algorithm distinguishes between the crack-opening and the crack-closing deflection. Where the crack-opening deflection has a positive displacement regarding to the undeflected shape, the crack-closing deflection has negative displacements. The force in the crack-opening deflection needs to be converged to a negative displacement whereas the force in the crack-closing deflection needs to be converged to a positive displacement.

As the stiffness decreases, the resonance frequency decreases, as seen from equation 2.4.5. This means that the steady state response of the displacement will shift. For the crack-closing deflection, the frequency slightly larger than the resonance frequency can be used as an excitation frequency. During crack-propagation, the graph will shift to the left and the magnitude of the displacement will decrease. Therefore, the force must be increased to satisfy displacement-control.

However, for the crack-opening deflection that means that the frequency directly lower than the resonance frequency ($\omega_{exc,1}$ = 72.34 Hz) cannot be used. As the graph will shift to the left, this will result in a jump from the crack-opening into the crack-closing deflection. As an alternative, the nodeset has been opened for the maximum amount of nodes, 40 nodes to the left and 40 nodes to the right. This results in an extreme scenario where the stiffness is at it's lowest point. Now, from here the excitation frequency is set slightly lower than the minimum value ($\omega_{exc,2}$ = 70.09 Hz). This means as the delamination increases in size, the graph will shift to the right and will not surpass the point that the ODS will jump from the crack-opening to the crack-closing deflection. A limitation to this approach is that the excitation frequency is relatively far from the resonance frequency. This means that the system does not fully make us of the potential sensitivitiy of the phase. As it excites further from the rensonance frequency, the drop in phase is smaller.

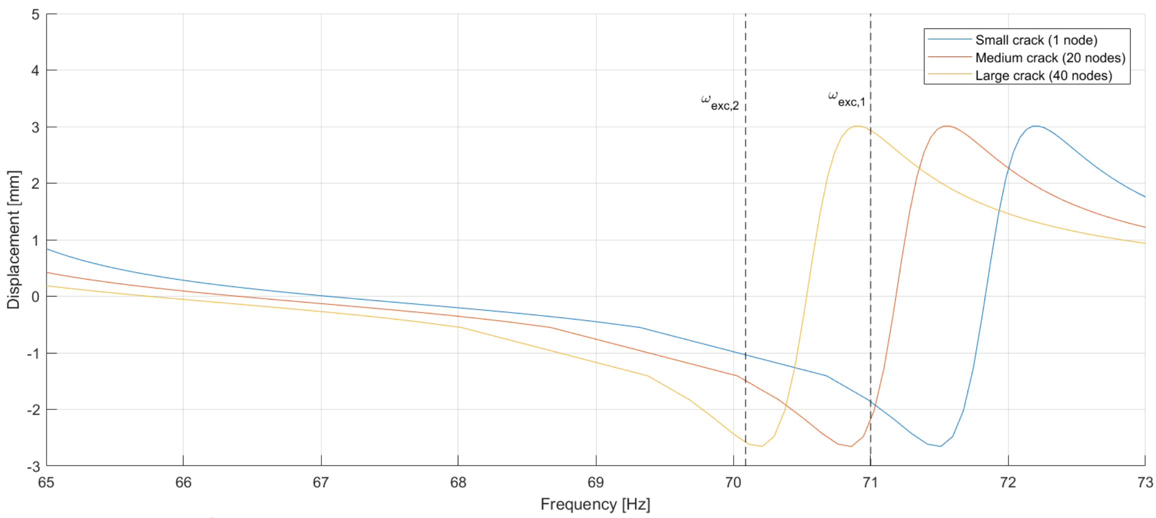

Figure 4.7: Steady state dynamic response for a small, medium and large crack length.

When the SSD analysis has run, the dynamic properties of the dynamic response can be obtained: the phase plot, the real part of the magnitude plot and the eigenfrequency. This data is saved for later processing.

Then, for the first iteration, the displacement does not have to be converged to the reference displacement, as it ís the reference displacement. So for the first iteration, the displacement solver is redundant and the deflection shape will be transferred to the static.

With the information provided from the SERR analysis, the bonded node set will be updated. As the crack will grow either to the right, the left, or in both directions. This will be the second iteration, the crack-modeling procedure will be repeated with a new bonded node set since the crack has grown. The new bonded node set, with the larger crack will result in a lower stiffness of the structure and thus a lower force required to maintain the same reference displacement. The correct force to maintain displacement control will be obtained in the Displacement solver.

From the second iteration on, the crack is propagating by opening the next nodes in the SSD bonded node set. This new SSD bonded node set is then again submitted for the SSD analysis. The entire process starts over, resulting in the release of more nodes to replicate a crack growth, until the desired crack length has been reached, or when the force is decreased as much that there is not enough energy in the system to open the next node.

4.3 Transfer distributed nodal displacement

After the SSD analysis, the steady state shape will be transferred to the quasi-static environment in order to perform the VCCT analysis. As this analysis is not possible in the dynamic environment. The solution proposed is to export the displacements for each individual node. The total set of displacements for each node is called the distributed nodal displacement matrix. This distributed nodal displacement matrix is then imported as a boundary condition in the static environment.

However, when the entire set of nodes is exported, it is not yet possible to calculate the SERR. It is given that the crack runs along the interface nodes of the cutplies with the lowerpart. As the entire model is exported as a boundary condition, the nodes at the interface of the crack are constraint in all their degrees of freedom. This means, that when the SERR is calculated, there will be no displacement between the nodes. According to equations 2.6.2 and 2.6.3, the SERR will be 0 if the relative deflection is 0. As a solution, the lower nodes of the top plies needs to be released (as seen in figure 4.8) from the nodal displacement matrix until the crack tip. In this way, all the degrees of freedom for the these nodes are released and are able to displace in-plane. Now the SERR can be obtained with use of the VCCT analysis.

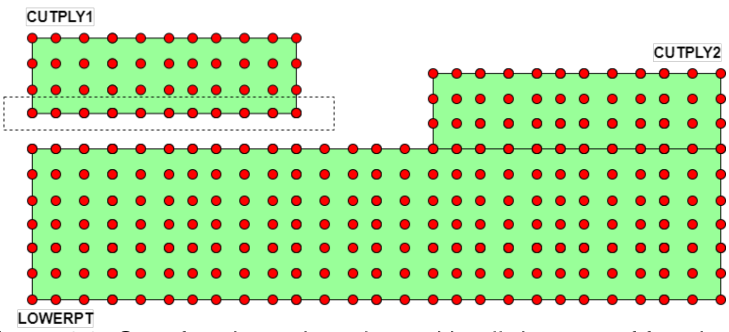

Figure 4.8: Set of nodes to be released in all degrees of freedom.

4.4 VCCT and SERR analysis

When the distributed nodal displacement is set as a boundary condition in the static environment, the VCCT analysis can be conducted. As described in section 2.6, the VCCT calculates the SERR by opening the nodes automatically. The initial bonded node set in the static environment consists of one node to the left and one node to the right. When the VCCT runs, the crack opens automatically, untill it reaches the first closed node in the dynamic bonded node set; the crack tip. This is the boundary condition in the static. Therefore, the VCCT analysis can not proceed and the SERR is calculated exactly at the crack tip. For both the right and left crack tip, the SERR values can be obtained: for the left crack tip $\mathrm{G}_{\mathrm{I,left}}$ and $\mathrm{G}_{\mathrm{II,left}}$ and for the right crack tip $\mathrm{G}_{\mathrm{I,right}}$ and $\mathrm{G}_{\mathrm{II,right}}$. A snapshot of the results from the VCCT analysis can be seen in figure 4.9. Here it can be seen that the SERR concentrates around the crack tip.

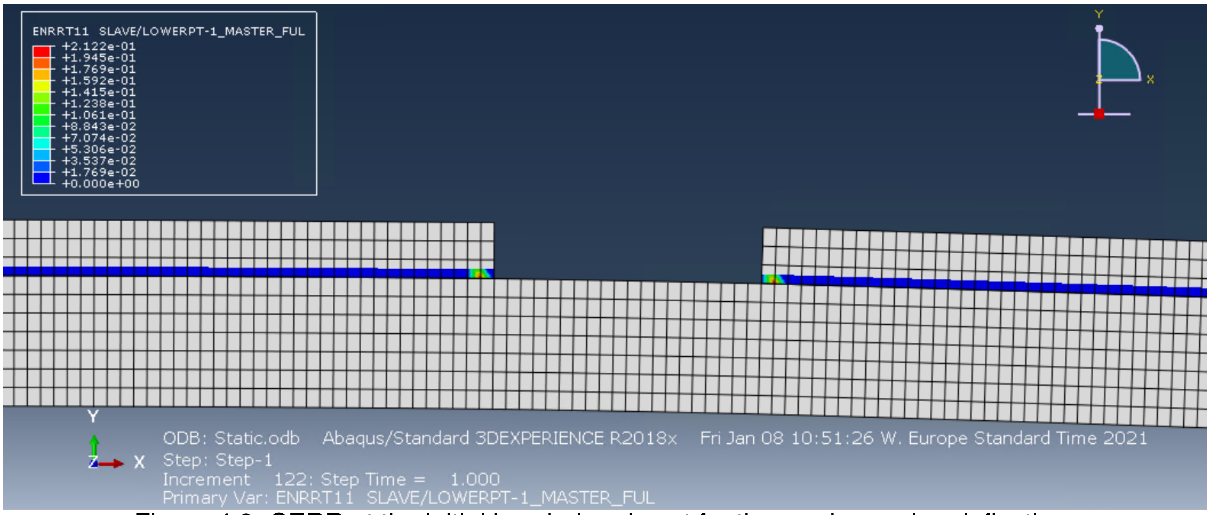

Figure 4.9: SERR at the initial bonded node set for the crack-opening deflection.

With the use of the SERR values, the mixed mode behaviour equivalent of the SERR can be obtained. Equations 2.6.5 and 2.6.6, can now be calculated. The crack tip node debonds when the fracture criterion of equation 2.6.4 reaches the value of 1.0. For both the left and the right crack tip, this debond criterion is calculated. On the basis of this data, it is decided to open the next node. When the criterion is not reached, the crack tip stays bonded. However, when the criterion is reached, the next node in the crack propagation will be opened manually in the SSD bonded node set.

Chapter 5

Crack-growth estimation

As the first objective is achieved, the second one will be to investigate the magnitude of the $\mathrm{G_I}$ and $\mathrm{G_{II}}$ for both opening and closing delamination. What are the differences in mode mixity between the crack-opening and crack-closing case? The goal is to understand the SERR changes for the positive and negative cycle of vibrations.

Furthermore, in this chapter, the numerical analysis will attempt to construct a relationship between the SERR and the vibration response phase over the total delamination length. The objective of this final attempt lies on the type of experiments carried out in the past, such as tracking the response phase during the fatigue tests.

During these experimental fatigue tests, it is found that there is a linear link between the slopes of the various segments in the phase trace and the crack growth ($\frac{\Delta a}{\Delta N} \propto \frac{\Delta \phi}{\Delta N}$) [7]. The phase-drop can be measured continuously and thus the $\frac{da}{dN}$ can be obtained. However, this is obtained by measuring the crack-length, either by X-ray CT scans or microscopic images, which are extremely time-consuming; three interrupted tests were used, running up to 250.000, 500.000 and 1.000.000 cycles, as seen in figure 5.1. After each test, the experiment was stopped to measure the crack-length. The graph shows interrupted measurements, the test has stopped 12 times, whereafter it was repeated. Therefore, the continuous curve of the graph could be constructed by superimposing the contributions of each interrupted test result. This results in a power curve. In the same graph, it can be seen that the phase-drop slope is overall the same for all three specimens over the number of cycles.

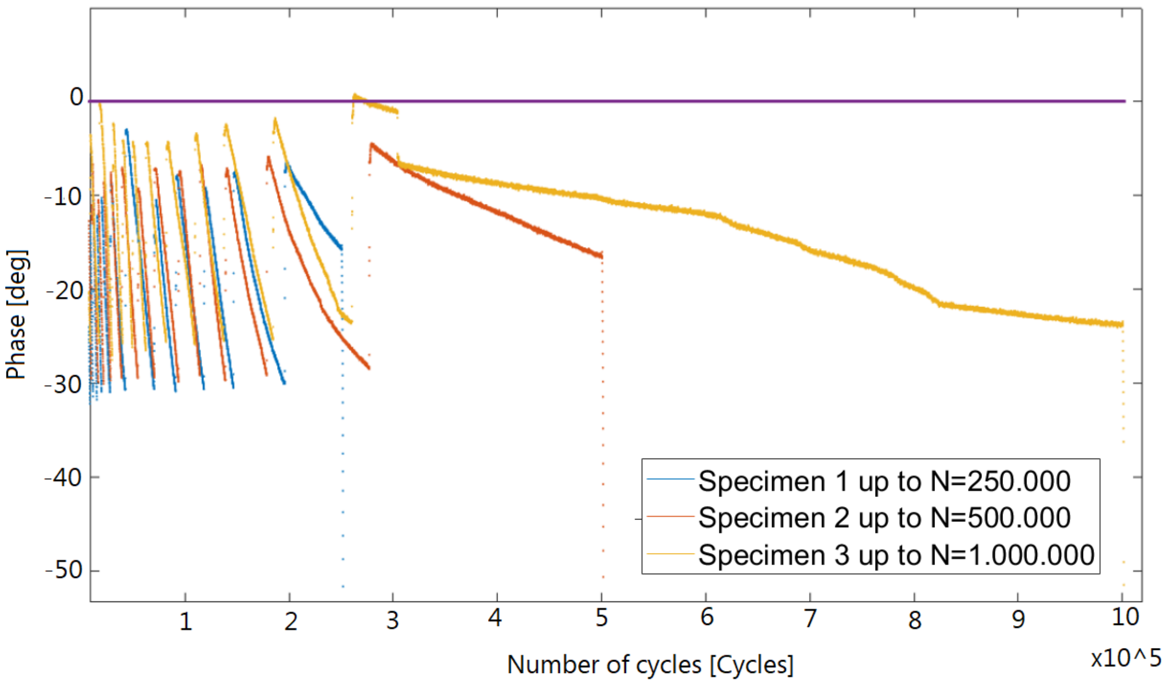

Figure 5.1: Interrupted test response phase for three specimen [7].

The results of the numerical contribution sheds new light on the determination of the equivalent SERR during experimental testing. One would like to know if the response phase measured experimentally can be converted by some sort of calibration factor or function into the equivalent SERR.

In order to come to the calibration factor, several research objectives are investigated; first the response phase is tracked for both the deflection shapes over the entire crack length. When the crack starts to grow, it induces a shift in the phase graph. At the constant excitation frequency, a drop in the phase is observed. This phase-drop is investigated secondly, showing a linear trend, which is in accordance to figure 5.1. Then the $\mathrm{G_I}$ and $\mathrm{G_{II}}$ are examined over the total crack length for both deflection shapes, resulting in a clear overview what the influences of $\mathrm{G_I}$ and $\mathrm{G_{II}}$ are to the total crack length. Finally, this results in the $\mathrm{G_I}$ and $\mathrm{G_{II}}$ related to the phase-drop over the entire crack length. With use of this data, the calibration factor can be constructed.

5.1 Delamination for the crack-opening deflection

In figures 5.2 and 5.3 an overview is presented of all the SERR values for the left and right crack length for the crack-opening deflection: $\mathrm{G_I}$, $\mathrm{G_{II}}$ and the total SERR $\mathrm{G_T}$. The individual contributions of the $\mathrm{G_I}$ and $\mathrm{G_{II}}$ to the $\mathrm{G_T}$ are presented by the blue and orange lines. Here it is obvious that the largest contribution comes from the $\mathrm{G_I}$ mode. In these graphs, it can be seen that when the $\mathrm{G_T}$ line becomes larger and crosses the $\mathrm{G_T^C}$, the crack grows. The crack-growth is binary, it grows 0.1 mm (size of the mesh) when $\mathrm{G_T} > \mathrm{G_T^C}$. The opposite is true as well: when the $\mathrm{G_T}$ is smaller than the $\mathrm{G_T^C}$, the crack does not grow. Thus if the threshold of $\mathrm{G_T^C}$ is not reached, there is no crack-growth. $\mathrm{G_T^C}$ is dependent on the parameters $\mathrm{G_I}$ and $\mathrm{G_{II}}$, and therefore, the threshold changes for every iteration. Crack-growth can be seen in figures 5.2 and 5.3 as an increasing crack length. When there is no crack growth, another iteration is needed at the same crack length; in the graphs, another data point is present for the same crack length. In figure 5.2, it can be seen that when the left crack starts to grow, the contribution of the $\mathrm{G_I}$ and $\mathrm{G_{II}}$ is approximately equal. Until the crack length reaches 0.4 mm, then the crack lengths is most influenced by the $\mathrm{G_I}$ mode. An explanation for the sudden drop after 0.4 mm must follow from a decreasing horizontal force. The remaining parameters, a, b follow from the geometry, which do not change and u_l does not change either, as the deflection shape remains the same. The growth of the right crack can be seen in figure 5.3, the $\mathrm{G_I}$ and $\mathrm{G_{II}}$ values show a similar tendency as for the left crack; when the crack is small, the contribution of the $\mathrm{G_{II}}$ is close to the contribution of the $\mathrm{G_I}$, but as the crack propagates, the influence of $\mathrm{G_I}$ appears dominant. Whether the crack has a tendency to grow more to a preferred direction - towards or away from the clamping side, can be seen in Appendix E.

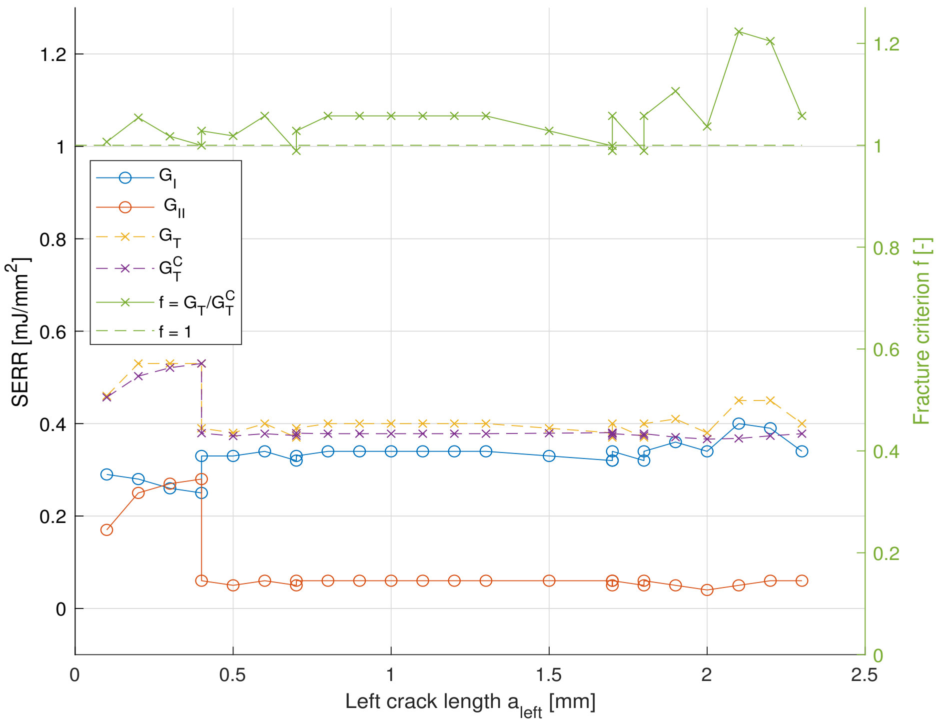

Figure 5.2: Contributions of the $\mathrm{G_I}$ and $\mathrm{G_{II}}$ to the $\mathrm{G_T}$ compared to $\mathrm{G_T^C}$ for the left crack length at the crack-opening deflection.

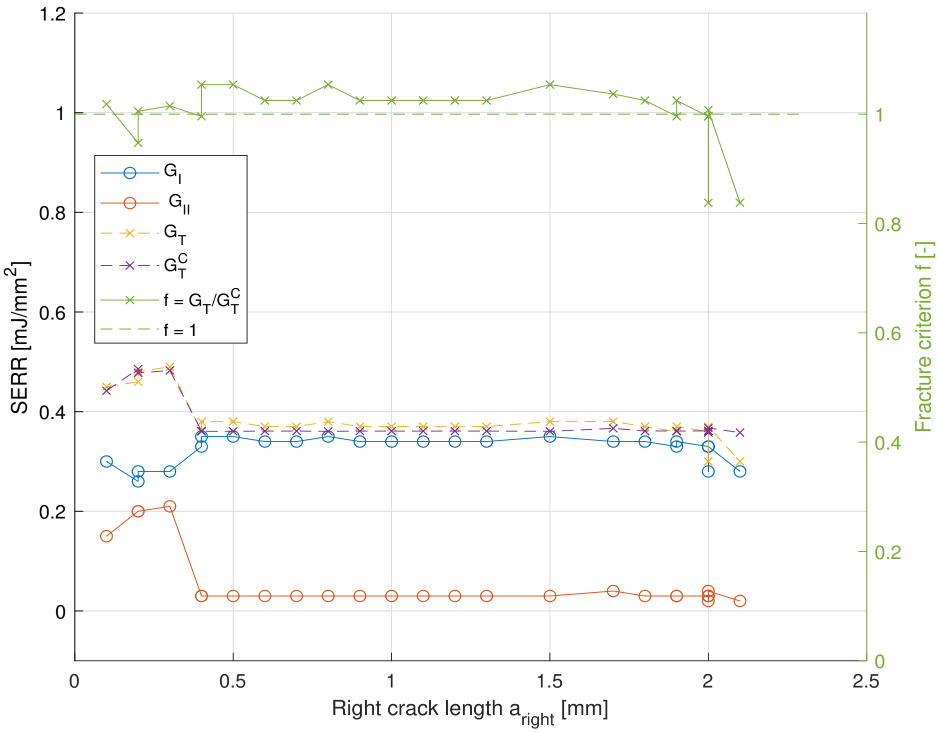

Figure 5.3: Contributions of the $\mathrm{G_I}$ and $\mathrm{G_{II}}$ to the $\mathrm{G_T}$ compared to $\mathrm{G_T^C}$ for the right crack length at the crack-opening deflection.

5.2 Delamination for the crack-closing deflection

In figures 5.4 and 5.5 an overview is presented of the SERR values for the left and right crack length for the crack-closing deflection. Again, the individual contributions of the $\mathrm{G_I}$ and $\mathrm{G_{II}}$ to the $\mathrm{G_T}$ are presented by the blue and orange lines. In the graphs, it is obvious that the only contribution to the $\mathrm{G_T}$ comes from $\mathrm{G_{II}}$. Therefore, $\mathrm{G_{II}} = \mathrm{G_T}$. This is an interesting phenomenon. It means that in the crack-closing deflection, the only contribution to the crack opening comes from the in-plane shear sliding mode. The crack does not grow as far as in the crack-opening deflection. After 0.7 mm propagation, that there is not enough strain energy in the system to open the crack. A larger severity level should result in a longer crack propagation. Whether the crack has a tendency to grow more to a preferred direction - towards or away from the clamping side, can be seen in Appendix E.

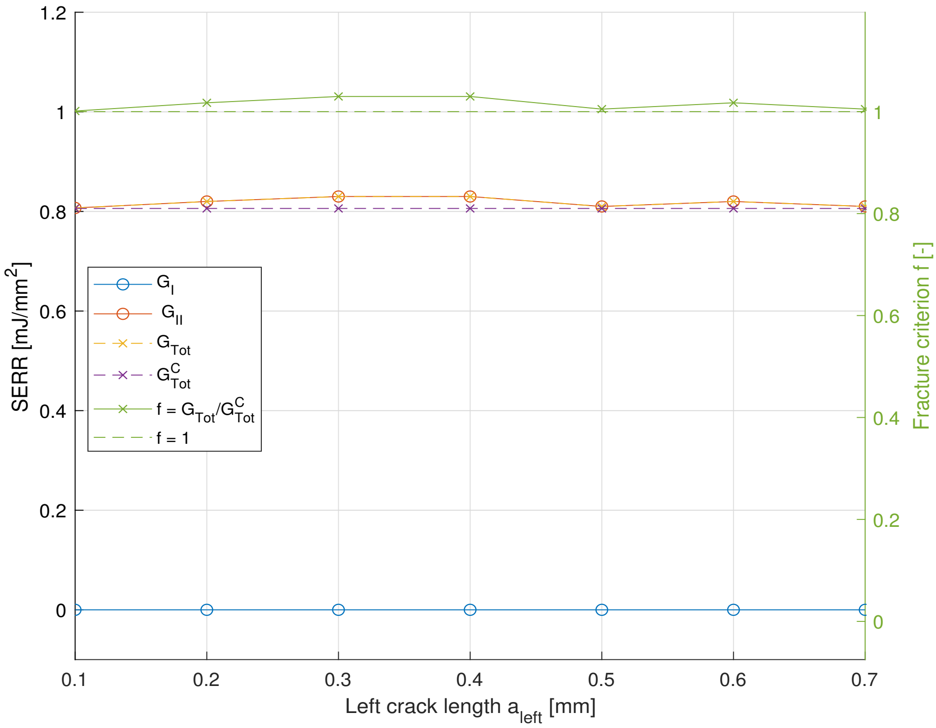

Figure 5.4: Contributions of the $\mathrm{G_I}$ and $\mathrm{G_{II}}$ to the $\mathrm{G_T}$ compared to $\mathrm{G_T^C}$ for the left crack length at the crack-closing deflection.

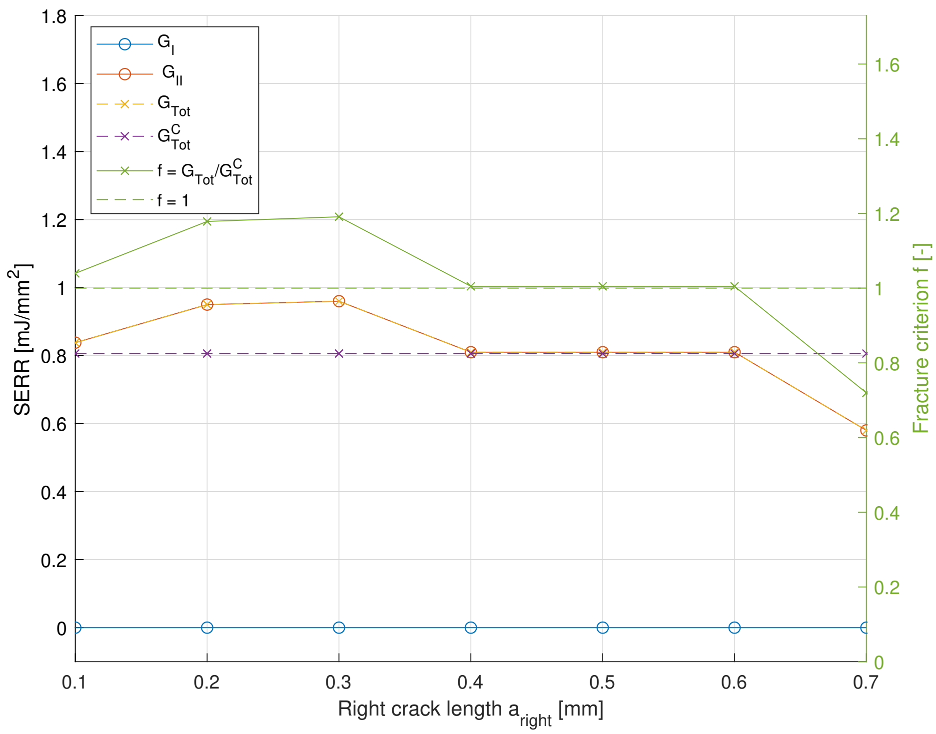

Figure 5.5: Contributions of the $\mathrm{G_I}$ and $\mathrm{G_{II}}$ to the $\mathrm{G_T}$ compared to $\mathrm{G_T^C}$ for the right crack length at the crack-closing deflection.

In figures 5.6a and 5.6b, the $\mathrm{G_I}$ and $\mathrm{G_{II}}$ is plotted over the total crack length. Note that in figure 5.6b, $G_T = G_{II}$, due to the absence of a contribution of G_I. This provides an insight in what the contribution of the G_I and G_{II} modes (mode mixity) are to the total crack onset. For the crack-opening deflection, when the crack is still small, until 0.7 mm, an equal combination of G_I and G_{II} results in the crack opening. Then, for larger crack openings, the contribution of the G_I remains the dominant mode opening to the total crack. This is the opposite for the crack-closing deflection, where, the G_I mode opening has no influence at all on the total crack opening. Only the contribution of the G_{II} sliding mode results in the opening of the crack. The mode mixity is different for both deflection shapes.

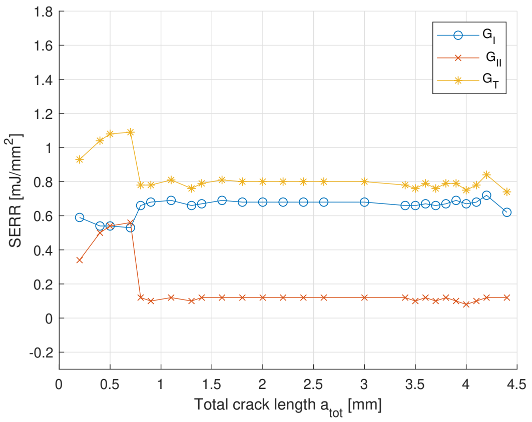

(a) SERR over the total cracklength for crack-opening deflection.

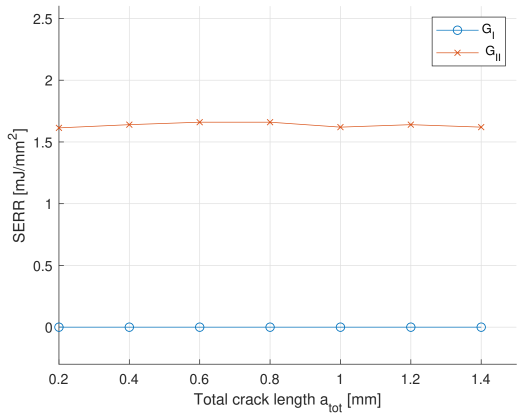

(b) SERR over the total cracklength for crack-closing deflection.

Figure 5.6: SERR over the cracklength for (a) the crack-opening and (b)crack-closing deflection.

5.3 Phase-drop during crack opening for the crack-opening and crack-closing deflection

The magnitude and phase diagrams obtain valuable information. As with the experiments, one would measure the amplitude and phase of the vibration. The FE simulation will report how those two functions are influenced by the crack propagation; a frequency shift of the graphs can elegantly be obtained. The crack growth shows that by increasing the delamination length the system dynamic response shifts towards lower frequencies, as expected. An example of these dynamic properties of the crack-opening deflection can be seen in figures 5.8a and 5.8b. The total crack length is used now, as any change in either the right or the left crack results in a stiffness degradation and thus in a phase-drop.

The excitation frequency is relative far from the resonance frequency, as a result of the extreme frequency phenomena. This means that the system does not fully make use of the potential sensitivity of the phase. As it excites far from the resonance frequency, the slope is smaller. However, the graph shifts towards the excitation frequency, which implies that the slope will become larger, when the crack grows. In the graph, it can also be seen that the displacement at the reference point is constant. This is due to the fact that the displacement algorithm adjusts for displacement control. For increasing crack lengths, the magnitude of the force needs to be decreased. This means that the reel part of the the displacement will become smaller when the crack propagates.

Unfortunately, the results are slightly discontinuous from the excitation frequency until approximately 70.9 Hz. The results, however do show the correct tendency and the correct convergence to the reference displacement - at the excitation frequency all the magnitudes go through -0.954 $\pm$ 1 $\%$ mm. The same shift in frequency also holds for the phase plot. It can be seen that the phase plot shifts to a lower frequency when more nodes are opened, thus when the total crack grows.

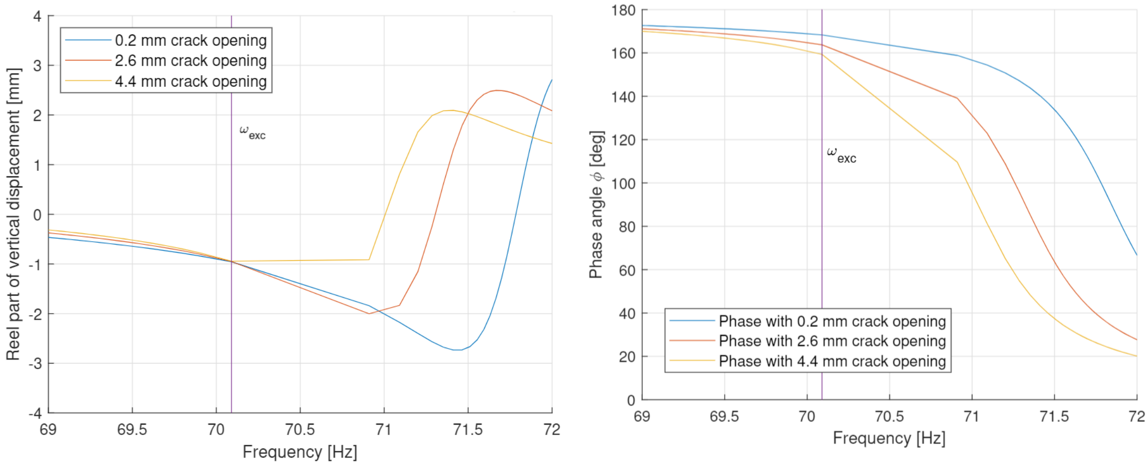

(a) Real part of the generalized displacement U2.
(b) Phase angles of the generalized displacement U2.

Figure 5.7: Dynamic properties of the crack-opening deflection for three crack lengths with (a) The reel part of the magnitude of the vertical displacement and (b) The generalized phase angles of the vertical displacement.

The crack-closing deflection looks similar, only with the excitation frequency closer to the resonance frequency: at 72.34 Hz instead of 70.09 Hz (purple vertical line in plot). Also with a smaller total crack length (a_{tot}), as less iterations are performed for the crack-closing deflection. Again, the results are slightly discontinuous. A possible explanation for this is a relative small discretization of the sample frequency or a too large mesh size, as discretization may have a large impact. The results, however do show the correct tendency and the correct convergence to the reference displacement - at the excitation frequency all the magnitudes go through +0.954±1 mm. Contrary to the crack-opening deflection, the excitation frequency is relatively close to the resonance frequency. So it has a higher sensitivity.

When the graph shifts, the resonance frequency will drift away from the excitation frequency; this implies that the slope and thus the sensitivity will become smaller, when the crack grows. For increasing crack lengths, the magnitude of the force needs to be increased.

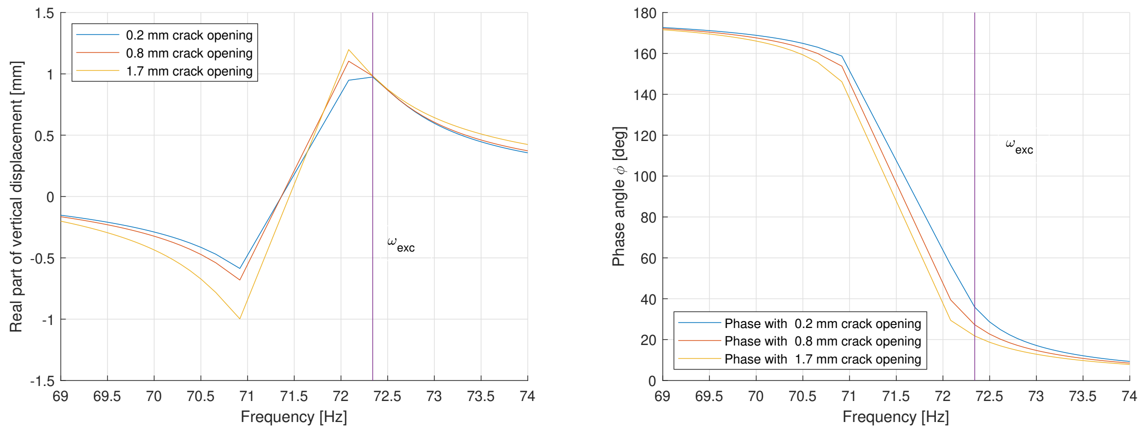

(a) Real part of the generalized displacement U2.
(b) Phase angles of the generalized displacement U2.

Figure 5.8: Dynamic properties of the crack-closing deflection for three crack lengths with (a) The reel part of the magnitude of the vertical displacement and (b) The generalized phase angles of the vertical displacement.

From the phase plot, the phase-drop can be obtained, for both the crack-closing and crack-opening deflection. The phase-drop is the amount the phase angle drops during the crack growth at the excitation frequency. In figures 5.9a and 5.9b the percentage change of phase-angles over the cracklengths are represented. In the same graph, the percentage change of the resonance frequency is highlighted too. These are calculated by,

$$Phase\ \ Degradation = \frac{\phi}{\phi_{initial}} * 100\% - 100 \tag{5.3.1}$$

and

$$Resonance\ \ Degradation = \frac{\omega_r}{\omega_{r,initial}} * 100\% - 100 \tag{5.3.2}$$

It can be seen that the slope of the resonance frequency is less steep than the slope of the phase angle at the excitation frequency; for the crack-opening deflection, the phase angle drops 9 degrees, whereas the resonance frequency drops only 0.8 degrees. The phase angle is thus 11.3 times more sensitive to change. The same holds for the crack-closing deflection, when the phase angle drops 14 degrees, the resonance frequency shifts 0.4 degrees. Which means the phase is 35 times more sensitive to change. Therefore, the phase angle is more suitable for measuring the crack opening accurately. The linear degradations do not show a perfect line. A reason for this is the discontinuities in the phase plots.

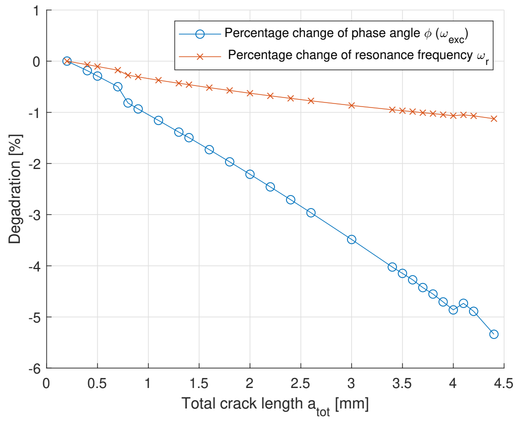

(a) Phase angle over the cracklength for crack-opening deflection.

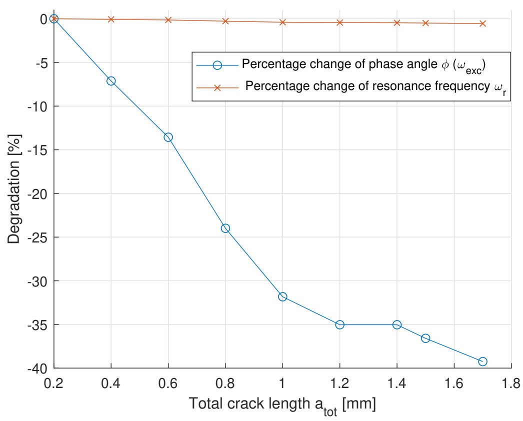

(b) Phase angle over the cracklength for crack-closing deflection.

Figure 5.9: Phase angle over the cracklength for (a) the crack-opening and (b)crack-closing deflection.

Then, in figures 5.10a and 5.10b, the phase-drop is plotted over the total crack length. For both the crack-opening and crack-closing deflection, the phase-drops appear to be relatively constant in both cases. The phase drop is the difference between subsequent points, as $\phi_{n+1} - \phi_n$.

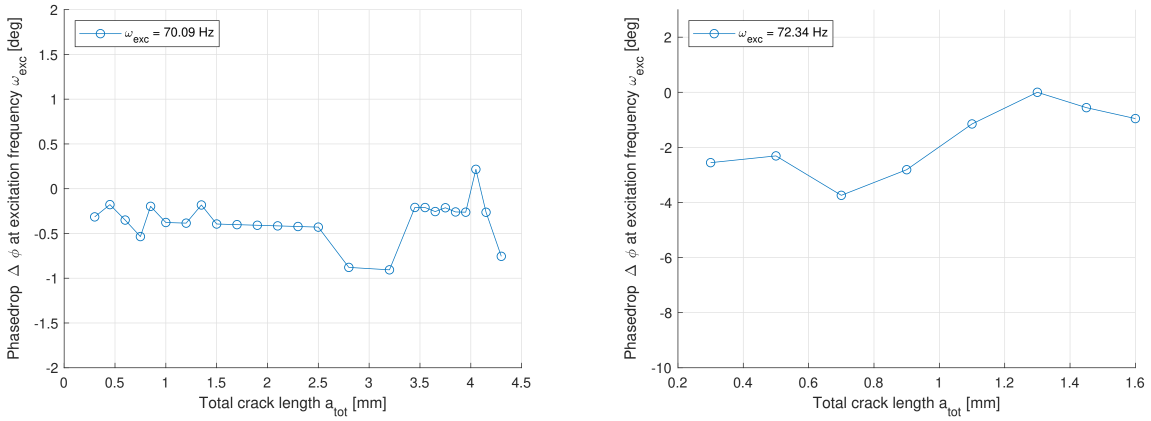

(a) Phase-drop over the cracklength for crack-opening deflection.

(b) Phase-drop over the cracklength for crack-closing deflection.

Figure 5.10: Phase-drop over the cracklength for (a) the crack-opening and (b)crack-closing deflection.

5.4 Correlation between the SERR and phase-drop for crack-opening and crack-closing deflection

Finally, the two plots of figures 5.10 and 5.6 are combined.The SERR is plotted against the phase-drop in figure 5.11.

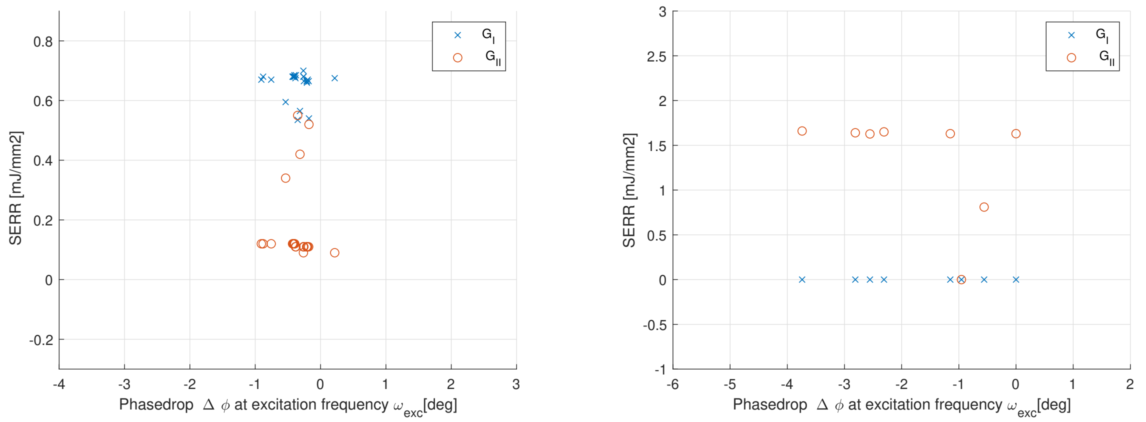

(a) SERR over the phase-drop for crack-opening deflection.

(b) SERR over the phase-drop for crack-closing deflection.

Figure 5.11: SERR over the phase-drop for (a) the crack-opening and (b)crack-closing deflection.

For the crack-opening deflection, it can be seen that for small phase-drops (0 - 1°), the SERR values are clustered and constant. For small phase-drops the absolute values for $\mathrm{G_I}$ an $\mathrm{G_{II}}$ are known. Thus it is also known in what extent the the mode I and mode II play a role in the crack opening.

Lastly, for the crack-closing deflection, mode I does not play a role, thus the full crack opening will be dominated by mode II. In figure 5.11, it can again and also be seen that for small phase-drops (0 - 4 °) the $\mathrm{G_{II}}$ value is relatively constant. Thus for small drops in the phase, it is known what absolute value $\mathrm{G_{II}}$ has.

The $\mathrm{G_I}$, $\mathrm{G_{II}}$ (and thus $\mathrm{G_T}$) values can be obtained for small phase-drops. This means that the $\left(\frac{G_T}{\Delta\phi}\right)_{num}$ can then be used as a novel calibration factor to find the total SERR during experimental testing, as follows,

$$\Delta\phi_{exp}\left(\frac{G_T}{\Delta\phi}\right)_{num} = G_{T,exp} \tag{5.4.1}$$

Where $\left(\frac{G_T}{\Delta\phi}\right)_{num}$ is the calibration factor obtained from the numerical framework. In practical terms, this means that with this calibration, it is possible while performing the experimental tests, to directly gain enough information about the value for $\mathrm{G_T}$. As the phase-drop can be continuously measured during the experiments, there is direct continuous information what the total SERR value will be, only by measuring the phase-drop. Also the real time information of the experimental $\mathrm{G_T}$ parameter could be beneficial for further investigation in bending mechanics.

Chapter 6

Conclusion and recommendations

This thesis, titled “Investigation of delamination crack under vibration fatigue exploiting simulation aided dynamic testing in digital environment”, aimed at studying the following main research question:

“What are the contributions of failure modes I II to the delamination growth under vibration loading conditions and how can this be modelled efficiently by a new numerical model including contact elements to simulate friction effects in the delamination area?”

Answers to this research question are found by investigating the following research objectives:

- The first objective is primarily to develop a framework to investigate the forces at the crack tip acting at two ends of the delamination. It will show how an experimental test can be break down by finite element analysis to allow such investigation.

- The second one is to investigate the magnitude of the $\mathrm{G_I}$ and $\mathrm{G_{II}}$ for both opening and closing delamination. What are the differences in mode mixity between the crack-opening and crack-closing case?

- Lastly, the numerical analysis is to attempt to construct a relationship between the SERR and the vibration response phase over the total delamination length.

6.1 Conclusions

To begin with, the first research objective is being investigated. A new numerical model including surface elements in between the crack area is developed. The model simulates interlaminar friction effects, which has not been done before yet. The model is based on a VCCT inside the ABAQUS environment; developed with use of bonded node sets. Moreover, the model uses a very small initial delamination length (0.1 mm). The model uses a remastered method to simulate the displacement-controlled crack-growth under steady state loading conditions. The new numerical model is used in a complex crack-growth modelling procedure. This framework investigates the forces at the crack tip, that act at the two ends of the delamination. The two ends of the delamination are investigated under two cases; the crack-opening and crack-closing deflection shape. However, the method makes use of two frequencies to capture these deflection shape. This is a pragmatic approach, which does not exactly match with the experiments. Moreover, to capture the displacement, solely the real part of the magnitude is used, which does not represents the total displacement of the structure.

In order to raise answers to the second research objective, first the crack lengths are identified for both the crack-opening and crack-closing deflection. With a reference to Appendix E, it is possible to see how the crack grows, whether it opens more to the clamping side(left) or away from the clamping side (right). Two cases are investigated by means of steady state, time-independent testing: the crack-opening deflection and the crack-closing deflection. For the crack-opening deflection, the crack grows 2.2 mm to the left and 1.9 mm to the right. For the crack-closing deflection, the crack grows 0.8 mm to the left and 0.7 mm to the left. It can be concluded, that the crack will grow faster to the clamped side, as both cases grow more to the left than to the right, this is in accordance with literature. With a note that these are time-independent tests.

Then, the relationship between phase-drop and resonance decay is underlined. Contrary to the previous research objective, instead of investigating the left and right crack, here the phase is related against the total crack length. As a crack in either the left or right crack results in a stiffness decay and thus in a resonance frequency shift. The phase angle has a higher sensitivity to change; a small change in the crack length gives a larger drop in the phase angle than in the resonance frequency and could thus be used as a sensitive parameter in the crack-growth analysis. The phase-drops appear to be relatively constant in both cases, for both the crack-opening and crack-closing deflection. However, in experimental tests, a power curve has been obtained. A reason for the discrepancy is that the excitation frequencies are relatively far off-resonance, where the tangent function of the phase becomes shallow. The phase drops relatively less compared with the phase drop at the resonance frequency. Which could be the reason that a linear phasedrop can be obtained instead of a power curve.

Finally, the SERR is related to the crack-length for two cases in the fully reverse cycle of R = -1; when the structure is vibrating, the structure vibrates from the crack-closing deflection to the crack-opening deflection. This means that in the vibration a discrepancy in the mode-mixity can be observed: the crack-closing deflection has a different effect to the crack growth than the crack-opening deflection; for the crack-opening deflection, the $\mathrm{G_I}$ has the most dominant influence to the $\mathrm{G_T}$. However a combination of both $\mathrm{G_I}$ and $\mathrm{G_{II}}$ results in the crack growth. For the crack-closing deflection, it can be concluded that mode I does not have any contribution to the crack length. This means that, for opening the crack, all the strain energy comes from mode II: the in-plane shear sliding mode. Mode II, the bending mode has no effect to the crack opening. It can be concluded that the mode-mixity varies between the two deflection shapes within the fully reverse cycle.

Lastly, the third research objective is investigated by relating the SERR to the phase-drop. In these results, for small phasedrops, the data points cluster. This means that for small phase-drops, the $\mathrm{G_T}$ could be estimated by a novel numerical calibration factor $\left(\frac{G_{Tot}}{\Delta\phi}\right)_{num}$. With use of this calibration factor, the experimental $\mathrm{G_T}$ can be derived at any given moment as the experimental phase-drop is always known. It can be concluded that the derivation of the $\mathrm{G_T}$ from the same vibration response phase has been accomplished. Besides the real time SERR values can be of interest for further investigation in bending mechanics.

These research objectives give a broader understanding in the physical phenomena underneath the delamination crack under vibration fatigue. By obtaining a more profound understanding in the physics, the results of the experiments can be analyzed in a better way. This thesis represents a solid starting point to elaborate on fracture mechanics investigation, especially for aerospace industrial application where time saving, efficient and innovative techniques are required.

6.2 Recommendations

All things considered, this research has several aspects that can be improved.
First of all, this study introduced a novel numerical model for characterising the delamination crack under vibration fatigue. The new model includes surface elements in between the crack area and has a very small initial delamination length. Regarding the new numerical model, in future research, the following three points should be considered. First, in the model, a hyperfine mesh has been used. But to identify the numerical error, a study of the mesh size to the FEA results should formally be performed. This could indicate whether the mesh needs to be refined and has the potential to obtain less discontinuities in the phase plots. Second, the transverse crack in the model is relatively large. In the next models, a smaller gap should be used. This corresponds better with the crack size in the experiments. And last, the friction coefficient should also be validated, even though, the experimental investigation of friction forces in a delaminated area could be extremely challenging.

With an eye on the crack-growth modelling process, a crucial improvement should be made. The current procedure is by means of a hybrid design: partly automated by an algorithm between MATLAB and ABAQUS and partly - very time consuming - manual work. A new procedure could more efficiently be automated with use of Python. Python has in-built properties in ABAQUS, which makes the interface much more convenient and manageable.

In the crack-growth modelling process, solely the real part of the magnitude has been used to measure the displacement. However, this is not correct and does not represent the actual displacement. In the next research, the magnitude of the displacement should be analyzed, which is a combination of the real and imaginary part of the displacement. Also, in the analysis, two excitation frequencies are used. However, this should be one and only one frequency; the resonance frequency should be the excitation frequency. In ABAQUS, a method should be acquired to obtain both the crack-opening and crack-closing deflection at the resonance frequency.

In this research, quantitative prediction of the SERR is not the aim of the analysis and is not the aim of this investigation as it requires a different set of modelling skills. For the correlation to become a causality, more experiments needs to be conducted. This can be done with different material parameters for the same severity level. Or use countless higher severity levels. Due to time consumption of the hybrid modelling, this was left to be done. When the process is fully automated, more severity levels could be introduced in the simulation driven dynamic testing environment. In this research only one severity level is used, while it is of an high interest to understand the crack-growth behaviour under different loading conditions. When the severity level is increased, the crack-length will also grow longer as there is more strain energy in the system. It is insightful to have more data from longer crack-lengths. This would result in more quantitative data, which makes the numerical calibration factor more accurate.

Last, a valuable addition to the simulations would be to perform transient simulations. The current simulations are performed under steady state assumptions, independent of time. However in reality the crack growth is strongly dependent on time. Time-dependent simulations will provide more data through the fully reversed cycle. In that case, the SERR values will be known throughout the entire vibration cycle. Whereas in this research, the SERR values are only known at the most deflecting mode shape. Although transient simulations are very time-consuming, it could uncover hidden time- or cycle-dependent relationships.

Bibliography

[1] Aerospace and Defense Technology. Thermoplastic composites to play enhanced role in next-generation aerospace applications. *Retrieved from https://www.aerodefensetech.com/component/content/article/adt/features/articles/34123* , August 5th 2020.

[2] F. Magi. *Vibration fatigue testing for identification of damage initiation in composites*. University of Bristol, 2016.

[3] P. Beaumont. *Physical modelling of damage development in structural composite materials under stress*. Cambridge University, 2003.

[4] ASTM international. *D6115 - 97 Standard Test Method for Mode I Fatigue Delamination Growth Onset of Unidirectional Fiber-Reinforced Polymer Matrix Composites*. World Trade Organization Technical Barriers to Trade (TBT) Committee, 2019.

[5] R. Buzzard, B. Gross, and J. Srawley. *Mode II Fatigue Crack Growth Specimen Development*. 1986.

[6] ASTM international. *D3846 - In-Plane Shear Strength of Reinforced Plastics1*. World Trade Organization Technical Barriers to Trade (TBT) Committee, 2019.

[7] M. Peluzzo. *Damage growth analysis and Paris' law derivation from vibration fatigue testing*. Università Politecnica delle Marche, 2018.

[8] W.D. Callister and D.G. Rethwisch. *Materials Science and Engineering*. Wiley, 8th edition, 2011.

[9] Thomas for industry. Comparison of thermoset versus thermoplastic materials. *Retrieved from https://www.thomasnet.com/articles/plastics-rubber/thermoset-vs-thermoplastics* , August 19th 2020.

[10] Dragonplate. Carbon fiber 101: What do isotropic, quasi-isotropic, and anisotropic mean? *Retrieved from https://dragonplate.com/* , january 5th 2021.

[11] E.K. Gamstedt and L.A. Berglund. Fatigue of thermoplastic composites. *Fatigue in Composites: Science and Technology of the Fatigue Response of Fibre-Reinforced Plastics*, pages 314–338, October 2003.

[12] G. Voudouris. *Fatigue behaviour of composites under vibration and thermal loading*. University of Bristol, 2019.

[13] K. Reifsnider. *Fatigue behavior of composite materials*, volume 16. International Journal of Fracture, 1980.

[14] M.j. Salkind. *Fatigue of composites*. American Society for Testing and Materials, 1972.

[15] A. Ciulo and M. Kachanov. *On Absence of Quantitative Correlations Between Strength and Stiffness in Microcracking Materials*. International Jour-nal of Fracture, 2010.

[16] Lomov, S.V. et al. *Experimental methodology of study of damage initiation and development in textile composites in uniaxial tensile test*. Composites Science and Technology, 2008.

[17] T.K. O'Brien. *Towards a Damage Tolerance Philosophy for Composite Materials and Structures*. Composite Materials: Testing and Design (Ninth Volume), 1990.

[18] G. D. Sims. *Fatigue test methods, problems and standards*. Fatigue in Composites, 2003.

[19] ISO 13003. *Fibre reinforced plastics - Determination of fatigue properties under cyclic loading conditions*. 2003.

[20] M. May and S. R. Hallett. *A combined model for initiation and propagation of damage under fatigue loading for cohesive interface elements*. Composites Part A: Applied Science and Manufacturing, 2010.

[21] M. May and S. R. Hallett. *An assessment of through-thickness shear tests for initiation of fatigue failure*. Composites Part A: Applied Science and Manufacturing, 2010.

[22] V.Alfred Franklin and Christopher Thankaiyan. Fracture energy estimation of dcb specimens made of glass/epoxy: An experimental study. *Advances in Materials Science and Engineering*, July 2013.

[23] M. Torkaman Asadi. *Fundamentals of Modal Testing*. Agilent Technologies, 2000.

[24] Abaqus documentation. *Direct-solution steady-state dynamic analysis*. MIT, 2021.

[25] Fabrizio Magi, Dario Di Maio, and Ibrahim Sever. Damage initiation and structural degradation through resonance vibration: Application to composite laminates in fatigue. August 2016.

[26] S. Karmakov, F. Cepero-Mejías, and J.L. Curiel-Sosa. Numerical analysis of the delamination in cfrp laminates: Vcct and xfem assessment. *Elsevier*, 2020.

[27] R. Martin. *Delamination fatigue*. Materials Engineering Research Laboratory, 2003.

[28] 1000logos. Matlab logo. *Retrieved from https://1000logos.net/matlab-logo/* , February 15th 2021.

[29] J. Schön. Coefficient of friction and wear of a carbon fiber epoxy matrix composite. *Wear*, 2004.

Chapter A

ABAQUS modelling

A.1 Modelling approach for both SSD and static environment

Module	User activity	steps
Part	Draw the 3 individual parts and set the correct dimension accordingly. The bottom part is named the LOWERPT, the top left part the CUTPLY_1 and the top right part the CUTPLY_2	Create part - 2D Planar - Deformable - Shell - Planar
	Use 'connected lines' in the sketch section to subdivide part in the amount of plies	
	Use 'connected lines' in the sketch section to subdivide part areas in an area for the refined mesh and coarse mesh	
	Define the Slave surface 1	Tools - Surface - Manager - Create - 'select bottom surface of Cutply_1'
	Define Slave surface 2	Tools - Surface - Manager - Create - 'select bottom surface of Cutply_2'
	Define MASTER surface 2	Tools - Surface - Manager - Create - 'select bottom surface of Cutply_2'
Property	Define two types of material, one for the 0 ply and one for the 90 ply. The 0 ply is named CFRP_0 and the 90 ply CFRP_90	Material manager - Create ...
	For CFRP_0: Define the mass density	General - Density - 'specify the mass density in the datasheet'
	For CFRP_0: Define the elasticity engineering constants	Mechanical - Elasticity - Elastic- Engineering constants - 'specify the engineering constants'
	For CFRP_90: Define the mass density	General - Density - 'specify the mass density in the datasheet'
	For CFRP_90: Define the interchange elasticity engineering constants, interchange direction 1 with direction 3, such that E1 = E3, nu 12 = nu32, etc. and interchange direction 3 with direction 1, such hat E3 = E1, nu13 =nu12, etc.	Mechanical - Elasticity - Elastic- Engineering constants - 'specify the engineering constants'
	Define two sections: one section for the CFRP_90 and one for the CFRP_0	Section manager - create ...

	For CFRP_0 material	Solid - Homogeneous - 'select CFRP_0' - toggle 'plane stress thicknes' and set the thickness in z-directi
	For CFRP_90 material	Solid - Homogeneous - 'select CFRP_90' - toggle 'plane stress thicknes' and set the thickness in z-directi
	Assign the material sections to the corresponding plies	Section assignment manager - create...
	For the 0 plies	Select ply 2 from both CUTPLY_1 and CUTPLY_2, and ply 1, ply 4, ply 6 from LOWERPT, according to the stacking sequence
	For the 90 plies	Select ply 1 and 3 from both CUTPLY_1 and CUTPLY_2, and ply 2, ply 3, ply 5 and ply 7 from LOWERPT, according to the stacking sequence
Assembly	Import all the parts	Create instance - select the 3 parts - Toggle 'auto-offset from other instances'
	Move the parts to the correct coordinates	Translate instances
	Define Slave surfaces	
Mesh	Select mesh element type	Assign element type ...
	Create CPS4R element	Select all the elements - 'Linear' Geometric order - Toggle: 'plane Stress' - Toggle: 'reduced integration'
	For the coarse regions in the LOWERPT, CUTPLY_1 and CUTPLY_2	Seed edges - Select the coarse mesh sections - adjust the approximate element size to obtain the requested coarse mesh size
	For the refined regions in the LOWERPT, CUTPLY_1 and CUTPLY_2	Seed edges - Select the fine mesh sections - adjust the approximate element size to obtain the requested fine mesh size
	Mesh part	Mesh part
Assembly	Create node set for the Force	Tools - Sets - Manager - create - Node Set - select the two nodes where the force is applied
	Create node set for the Displacement node	Tools - Sets - Manager - Create - Node set - select the one node which serves as reference for the displacement
	Create node set for the Bonded node set	Tools - Sets - Manager - create - Node Set - select the initial nodes which represent the initial crack between the LOWERPT and the CUTPLIES

A.2 Modelling approach SSD environment

Module	User activity	Steps
Step	Define the frequency step	Step manager - create - Linear Perturbation - Frequency - Number of eigenvalues requested: select value: *insert requested amount of eigenvalues* - NLgeom: 'off'
	Define SSD step	Step manager - create - Steady-state dynamics, Modal ...
	Set up frequency range	Basic - NLgeom: 'off' - Scale: 'linear' - toggle off: 'use eigenfrequencies to subdivide each frequency range' - Specify the frequency range and number of points in the data section
	Add damping	Damping - Specify damping over ranges of 'modes' - Structural - Toggle 'use structural damping data' - Specify the damping constant over the requested amount of eigenvalues
	Select field output	Field output manager...
	For the frequency	-Step: 'Frequency' - Preselected defaults - Toggle 'displacement / velocity / acceleration'
	For the SSD	Step: 'SSD' - select from list below - Toggle 'stresses, strains, displacement/velocity/acceleration, Forces/Reactions'
	Select History output for the SSD	History Output Manager - create - Step: 'SSD' - Select from list below - Toggle 'Displacement/Velocity/Acceleration
Interaction	Make tie constraint	Constraint manager - create - tie - master type: surface - 'select Master surface' - slave type: node region - 'select bonded node set'
Load	Apply load	load manager - create - step: SSD - Mechanical - Concentrated force - select 'force set'
	Apply BC	Boundary condition manager - create - step: Freq - mechanical - displacement/rotation - select 'BC set'

A.3 Modelling approach static environment

Module	User activity	steps
Step	Define the static step, this should be user-defined such that the increments are small enough to let the solver with the set force converges to a solution	Step manager - create - General - Static, general - Basic - NLgeom: ’off’ - Incrementation - Automatic - Maxium number of increments: 10000 - increment size: initial: 1e-6, minimum: 1e-20, maximum: 0.01
	Select Field output	Field output manager - Step: ’Static’ - Select from list below - Toggle ’Contact: CSTRESS, CDISP, CFORCE, CSTATUS, Failure: DBT, DBSF, OPENBC, ENRRT, EFENRRTR, BDSTAT’
	Select History output	History Output Manager - create - Step: ’Static’ - Select from list below - Toggle ’Energy’
Interaction	Define interaction property	Interaction property manager - create - Contact - Mechanical ...
	Involve No slip	- Tangential Behavior - Penalty - Friction Coefficient =0.1
	Involve Hard contact	- Normal behavior - Pressure overclosure = Hard contact
	Generate VCCT	- Fracture criterion - VCCT - Parallel - BK - Enable unstable crack propagation - fill out the critical energy release rates and the exponent
	Involve geometry	- Geometric properties - fill out the out of plane surface thickness

Chapter B

Numerical test to identify vibration-driven modelling is more suitable than DCB quasi-static modelling

The fracture mechanics characterization is done by standard test using hydraulic machines. The Double Cantilever Beam (DCB) tests are used to characterize the mode-I failure following the ASTM standards [4] [5]. The test method for mode-II testing is performed by the Double Notched Shear test or the Short Beam Shear test. [6]. Eventually, both mode-I and mode-II are superimposed to take into account the mode mixity ratio in real conditions vibration fatigue. However, aerospace loading environments are dynamic and not quasi-static as in the testing practices. Dynamic loads, the ones right beyond the first resonant mode of vibration can lead to self-heating conditions which make the assessment of the material behaviour time-temperature dependent. Therefore, those are limited to very low rates. However, the true nature of the internal forces under dynamic loads leading to fatigue might not be as simple as the linear superimposition summation.
In this appendix, a numerical test results in the quasi-static and dynamic environment is presented for the crack opening deflection. Initially, the force is build up in the dynamic analysis to identify the stress level for the crack to open. Then at this stress level, the stresses are compared under dynamic and under static excitations. Different values in the quasi-static approach versus the dynamic approach is a sign that the dynamic nature of the experimental test is such that a quasi-static approach to modelling is not appropriate and, instead, a modelling framework including the dynamic conditions is needed to study the fatigue behaviour.

B.1 Determining stress level for crack opening

In this section, several iterations of the steady state initial force are performed to find a initial force in the dynamic environment large enough to induce the crack-growth, such that $G_{total} > G_c$. With a reference to table B.1.1, it is found that a concentrated force of 0.3N is required to introduce crack-growth. Any force with a magnitude smaller than 0.3N results in a SERR value lower than the critical SERR. This means that the crack will not grow, not towards the clamp and not from the clamp.

		Iteration 1	Iteration 2	Iteration 3	Iteration 4
Force magnitude [N]		0.050	0.100	0.250	0.300
Status crackopening		open(1,1)	open(1,1)	open(1,1)	open(1,1)
Frequency [Hz]		70.09	70.09	70.09	70.09
Damping [Ns/m]		0.010	0.010	0.010	0.010
severity level d [mm]		-0.159	-0.317	-0.795	-0.954
GI $[mJ/mm^2]$	left	0.008	0.030	0.219	0.298
	right	0.005	0.022	0.131	0.171
GII $[mJ/mm^2]$	left	0.008	0.031	0.213	0.302
	right	0.004	0.021	0.115	0.152
G_{equiv} $[mJ/mm^2]$	left	0.013	0.050	0.341	0.462
	right	0.012	0.047	0.321	0.455
$G_{equiv,c}$ $[mJ/mm^2]$	left	0.463	0.470	0.462	0.456
	right	0.441	0.453	0.446	0.441
$G_{equiv}/G_{equiv,c}$ [-]	left	0.028	0.106	0.735	1.011
	right	0.027	0.103	0.717	1.018
$G_{equiv,left} > G_{equiv,c,left}$		no, close L	no, close L	no, close L	yes, open L
$G_{equiv,right} > G_{equiv,c,right}$		no, close R	no, close R	no, close R	yes, open R

Table B.1.1: Four iterations to find the severity level which is large enough to induce crack-growth

B.2 Compare stress distributions under steadystate and static excitations

This section will describe the comparison of stress distribution of the cross-ply sample when a deflection is achieved by dynamic and static loads. The objective is to evaluate the different stress conditions are the crack tip. The steadystate deflection is achieved by applying a forces and measuring a response from a target reference node. The static deflection is achieved by applying two forces which will delfect the beam meeting the same target diplacement at the referrence point.

B.2.1 Steady state deflection

The first bending mode shape will be examined and compared to the static. Then two reference points on both 45mm to the left and right from the clamping will be used to measure the deflection, as seen in figure B.1.

Figure B.1: Two reference points measuring the deflection; node 1347 is the left reference point and node 3689 is the right reference point

Two points are necessary, as the deflection is not completely symmetric due to the introduced crack. The left half part is deflecting more than the right half part. In order to obtain a similar shape, these two deflections will serve as the reference input for the static case. This deflection is reached by inducing a SSD force of $F = 0.3$N to the Force node set. The displacements of the U2 real part will be taken as a reference displacement for the static analysis. The maximum deflection of the deflection is at 71.51 Hz. At this frequency, the displacements for the left and right reference node are displayed in table B.2.1.

	U2 displacement @ f = 71.51 Hz [mm]
Left reference point	-5.782
Right reference point	-2.803

Table B.2.1: Real part of the U2 displacement for the left and right reference point

In the analysis, the stress tensors (σ_{11}, σ_{22}), as well as the von Mises stress ($\sigma_{vonMises}$) will be observed. These stresses are highlighted in table B.2.2.

	Stresses at left cracktip [MPa]	Stresses at right cracktip [MPa]
σ_{11}	507.2	499.7
σ_{22}	32.10	29.97
$\sigma_{vonMises}$	492.8	486.0

Table B.2.2: Stresses under steadystate excitations with F= 0.3N

B.2.2 Static deflection

In order to gain matching deflection shapes in the static case, there will be two forces induced on the specimen: both a negative vertical force on the left hand side, as well as on the right hand side of the clamping. A free body diagram can be seen in figure B.2.

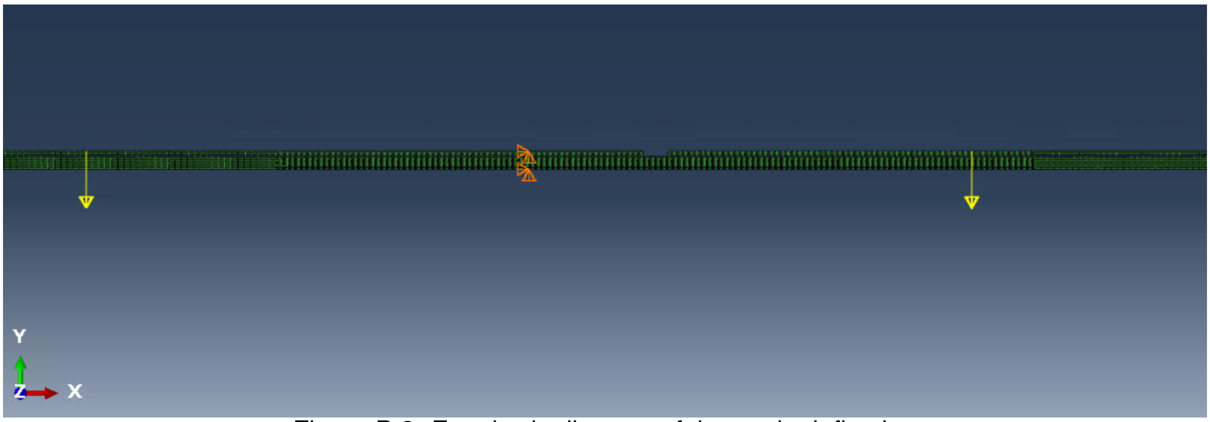

Figure B.2: Free body diagram of the static deflection

This force is iterated such that the reference node meets the deflection of the reference node in the dynamic case within a tolerance $< 0.5\%$. The force required to obtain the dynamic deflection and the deviation can be seen in table B.2.3.

	F [N]	Static displacement [mm]	Deviation w.r.t. steadystate displacement[$\%$]
Left reference point	-97	-5.816	0.588
Right reference point	-54	-2.790	0.464

Table B.2.3: Force required to reach the static displacement together with the deviation of the static and dynamic displacement

When the force is iterated such that the tolerance is met, the stress tensors (σ_{11}, σ_{22}), as well as the von Mises stress ($\sigma_{vonMises}$) are withdrawn, these can be seen in table B.2.4.

	Stresses at left cracktip [MPa]	Stresses at right cracktip [MPa]
σ_{11}	569.7	527.0
σ_{22}	37.20	30.49
$\sigma_{vonMises}$	553.2	512.9

Table B.2.4: Stresses under static excitations with F_{Left} = -97N and F_{Right} = -54N

The stresses in the left and right cracktip for under static excitations are now compared with the stresses under steadystate excitations in table B.2.5. Evaluating the stresses under the different condtions, it can be seen that all the stresses are larger under static excitations.

	Deviation between stresses static/dynamic at left cracktip [%]	Deviation between stresses static/dynamic at right cracktip [%]
σ_{11}	+12.3	+5.47
σ_{22}	+15.9	+1.73
$\sigma_{vonMises}$	+12.2	+5.55

Table B.2.5: Deviation in stresses under static and dynamic excitations for the left and right cracktip

B.2.3 Visualisation of the model due to dynamic and static excitations

The results of previous sections are now visualized. The bending shapes with one of the stress distributions (von Mises stress) can be seen in figure B.3. These numerical solutions show the bending shapes for both the dynamic and the static environment. Additionally, the two shapes are plotted on top of eachother in figure B.4. It appears that static gives a larger stress distribution than dynamic. However this does not give an identical mode shape. Therefore it could not be concluded yet that the static DCB tests are not a good representation for the dynamic environment in which aerospace applications are in. However, it gives an indication that dynamic testing modelling of onset delamintaion initiation appears more suitable. Therefore, the simulations will focus on vibration-driven crack growth.

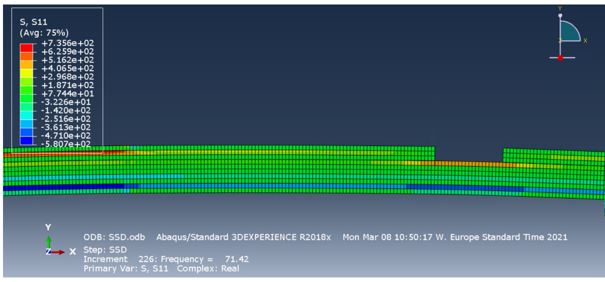

(a) σ_{11} under steadystate excitations

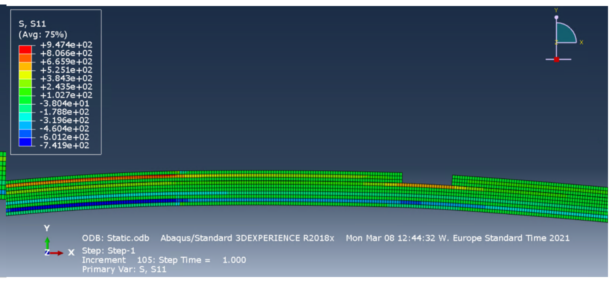

(b) σ_{11} under static excitations

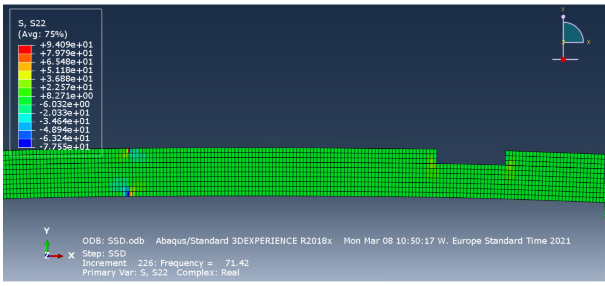

(c) σ_{22} under steadystate excitations

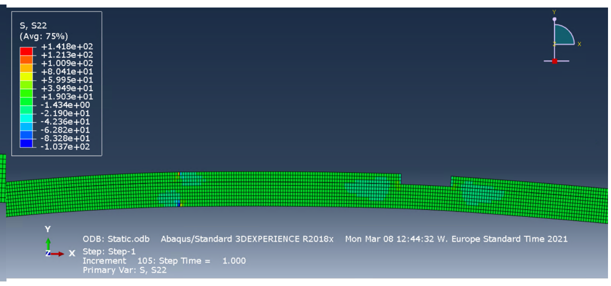

(d) σ_{22} under static excitations

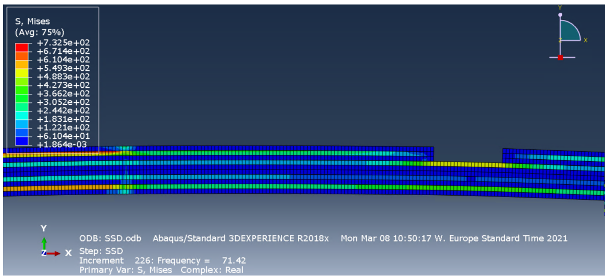

(e) $\sigma_{vonMises}$ under steadystate excitations

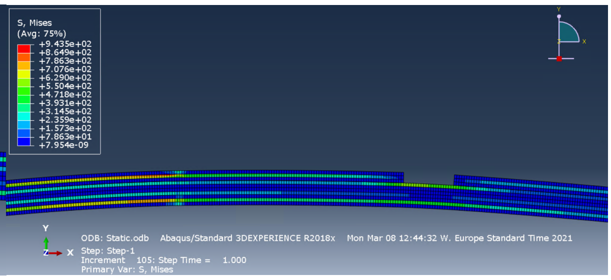

(f) $\sigma_{vonMises}$ under static excitations

Figure B.3: Two numerical solutions (a)(c)(e) Numerical solutions for the dynamic environment showing the dynamic stress distribution around the cracktips (b)(d)(f) Numerical solutions for the static environment showing the static stress distribution around the cracktips

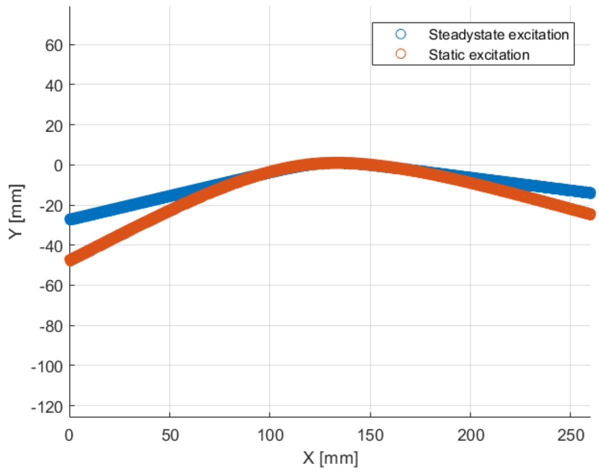

Figure B.4: Deflection shape under static excitation and dynamic excitation plotted together

Chapter C

Technical Drawingings parts

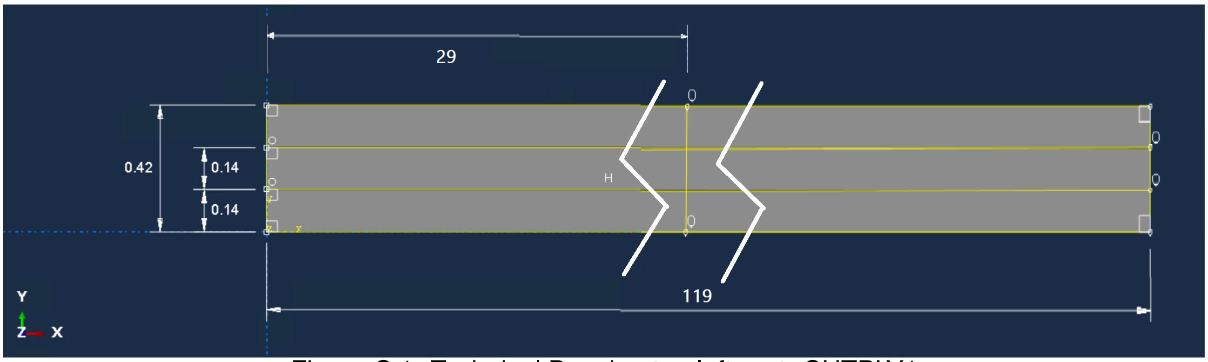

Figure C.1: Technical Drawing top left part: CUTPLY1

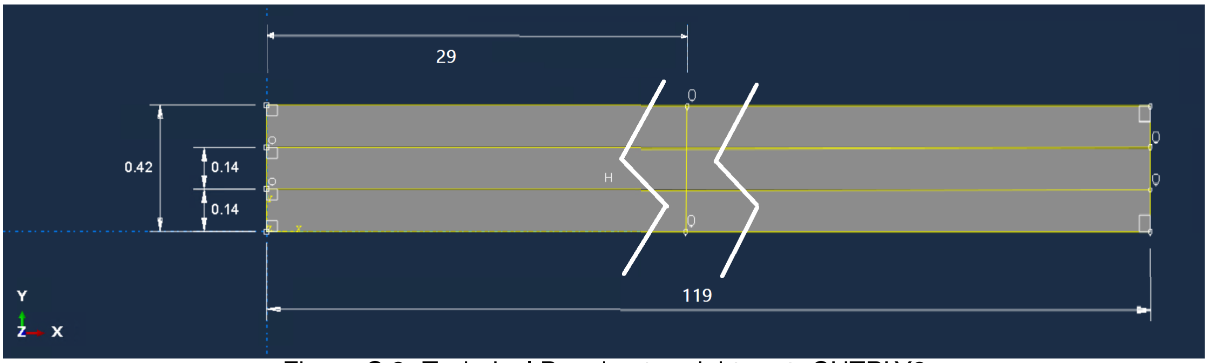

Figure C.2: Technical Drawing top right part: CUTPLY2

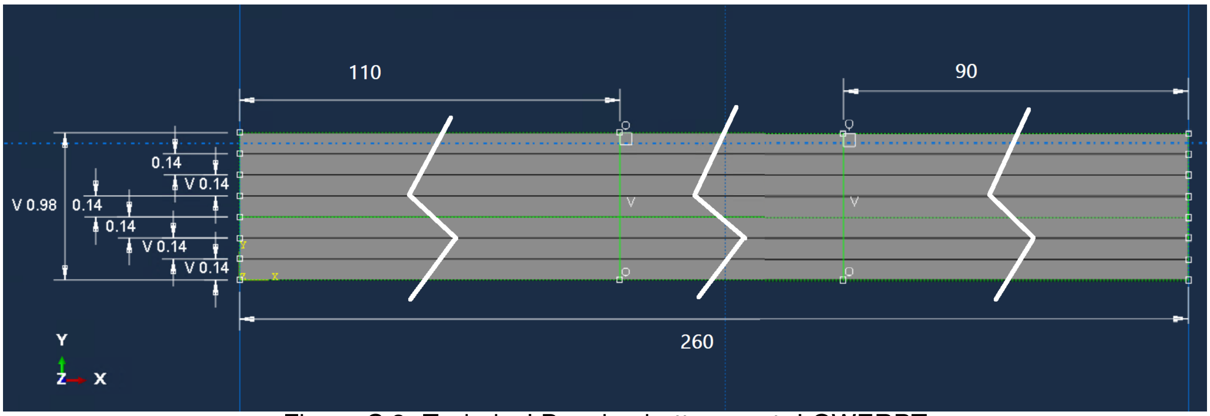

Figure C.3: Technical Drawing bottom part: LOWERPT

Chapter D

Individual components of the process flow

D.1 Initial model

Module	User activity	steps
Initial model	Find severity level	Iterate the force in untill it reaches the stress required for the severity level.

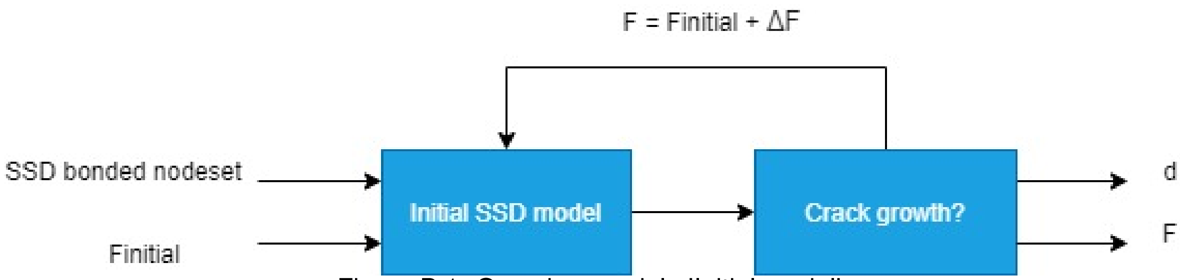

Figure D.1: Overview module 'Initial model'

D.2 Modal- and Steady State analysis

Module	User activity	steps
SSD	Run SSD	Run the model with the correct force obtained.
	Select real part	Result - options - complex form - real
	Select excitation frequency	Use the frame selector to guide to the increment of the requested excitation frequency
	Save the phase	Create XY data - ODB history output - phase angle of generalized acceleration: GP2 for whole model - Save to excel
	Save the magnitude	Create XY data - ODB field output - position: unique nodal - select: U: spatial displacement - in Elements/nodes select : Node sets : Part-1-1.Displacement_node - in Active Steps/frames: deselect the frequency step - Save the plot to excel
	Save the eigenfrequency	Results - Step/Frame - Frequency

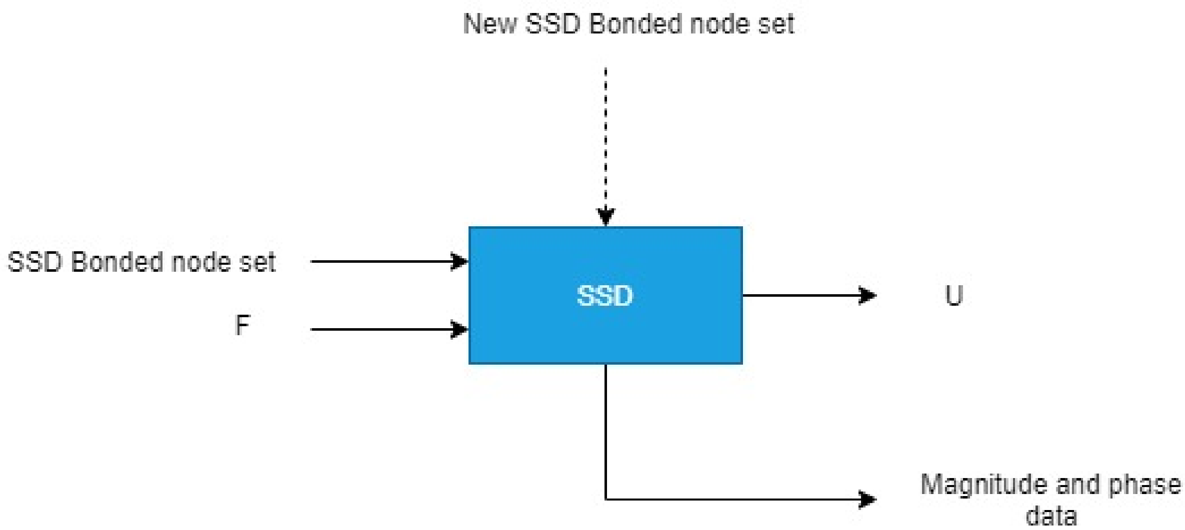

Figure D.2: Overview module 'Modal- and Steady State analysis'

D.3 Displacement Solver

Module	User activity	steps
Displacement Solver	Add displacement output in .dat file in order to automatically output the displacement value of the reference node to a data file	SSD model - keyeditor - add the lines from D.3 into the keyeditor
	Move .inp file	Copy the .inp file in the directory of the displacement solver
	Adjust force file	Adjust in the .inp the Force input from a fixed number, towards importing a force text file. Such that when Matlab overwrites the force textfile, a new force will be imported in the input file
	Set reference displacement	Adjust the reference displacement in Matlab to the reference displacement found in the initial model
	Run algorithm	Run the displacement solver algorithm

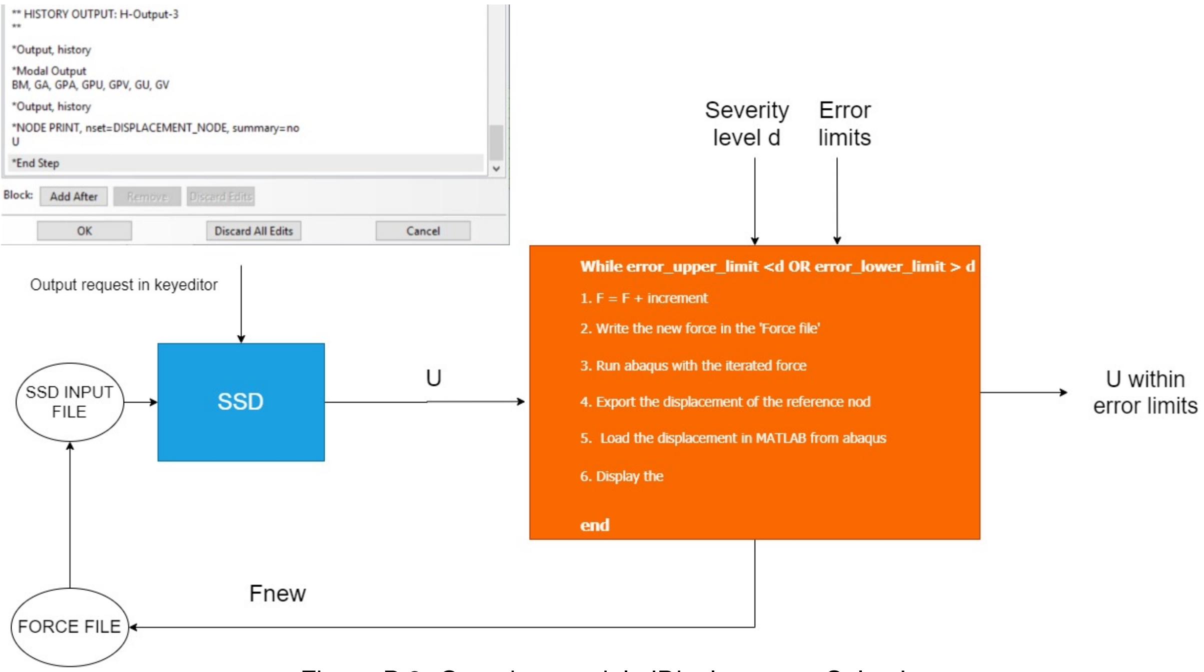

Figure D.3: Overview module 'Displacement Solver'

D.4 Transfer distributed nodal displacement from dynamic to quasi-static environment

Module	User activity	steps
Dynamic to Quasi-static	Request distributed nodal displacment to .rpt file	Report - field output - position: unique nodal - select: U: spatial displacement - in setup: deselect the append to file - save to .rpt
	Copy the nodes and it's displacements to columneditor Notpad++	Select all the nodes from 1-11936 and all the 4 columns
	Delete the overlapping nodes	
	Make U1 input	Transform the columns such that the following format is made: Node name, 1, 1, u1 displacement
	Mak U2 input	Transform the columns such that the following format is made: Node name, 2,2, displacement
	Include the U1 as a boundary condition in the static model	Go to static model - edit keywords - under *boundary copy the text: '*include, input = Directory\name_u1.rpt
	Include the U2 as a boundary condition in the static model	Go to static model - edit keywords - under *boundary copy the text: '*include, input = Directory\name_u2.rpt

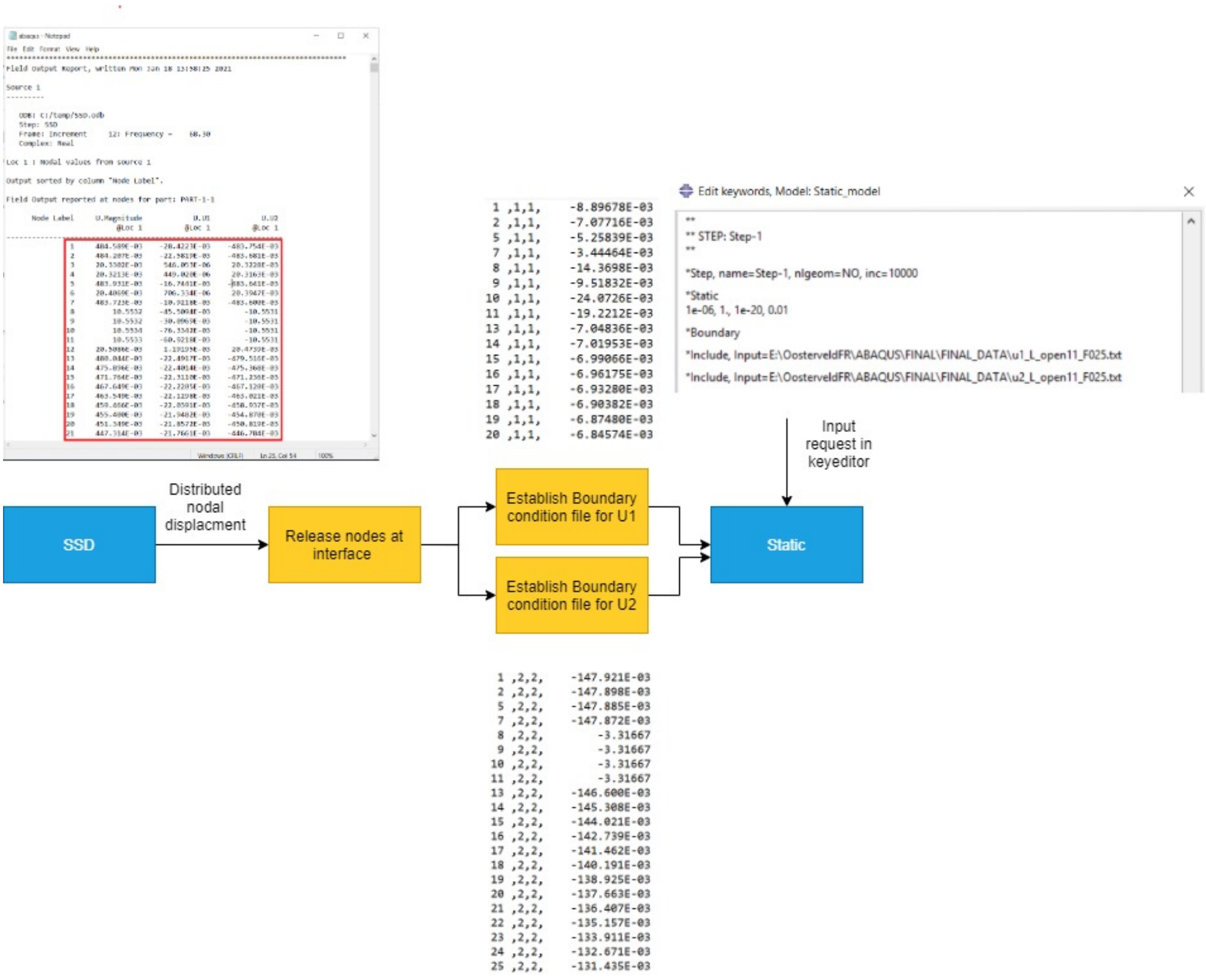

Figure D.4: Overview module Transfer distributed nodal displacement from dynamic to static environment

D.5 VCCT analysis

Module	User activity	steps
VCCT analysis	Run static model	Run the static model with the new boundary conditions
	Save G1 for left and right cracktip	Select Primary - ENRRT11 - Probe values - select the nodes at the cracktips for the left and right cracktip by using the key-in label
	Save G2 for right and left cracktip	Select Primary - ENRRT12 - Probe values - select the nodes at the cracktips for the left and right cracktip by using the key-in label

Figure D.5: Overview module 'VCCT analysis'

D.6 SERR analysis

Module	User activity	steps
SERR calculation	Calculate mixed mode behaviour G_{equiv} Calculate mixed mode behaviour $G_{equiv,c}$ Determine crack propagation	calculate G_{equiv} calculate $G_{equiv,c}$ Determine if $\frac{G_{equiv}}{G_{equiv,c}}$ is larger or smaller than 1

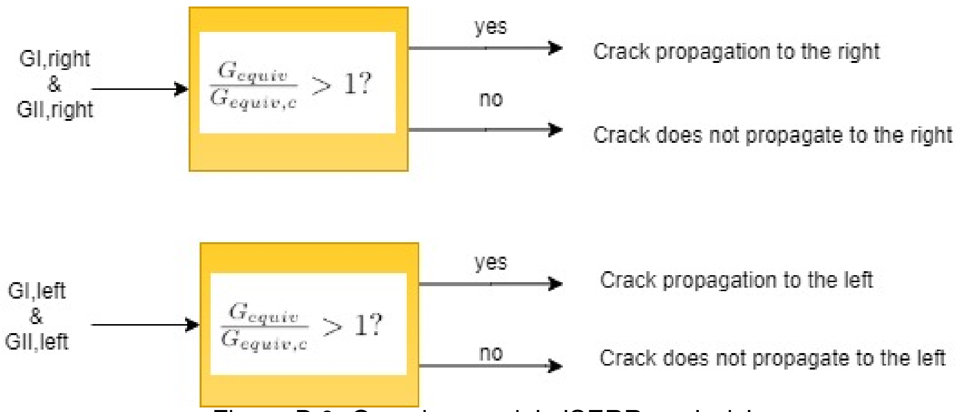

Figure D.6: Overview module 'SERR analysis'

D.7 New model

Module	User activity	steps
New model	Open new nodes in the new bonded-node-set according to the new crack propagation	In the SSD model - assembly - tools - sets - manager - bonded node set - open the new nodes according to the crack propagation criterion.

Chapter E

Crack growth direction under crack-opening and crack-closing deflection

In this Appendix, the crack growth direction is investigated for both the crack-opening and crack-closing deflection. In these simulations, it must be noted that these simulations are time-temperature independent. Time effects are neglected. In order to investigate the full influence and determination of the crack-direction, a more complex transient analysis is recommended.

E.1 Crack growth direction under crack-opening deflection

Whether the crack grows to the right, to the left (respectively from or towards the clamp) or in both directions, can be seen in figure E.1. In total, 27 iterations of the crack-modelling procedure are performed to check whether the crack should grow in the left or right direction for the crack-opening deflection. This could be extended as the left crack should still be opened at the last iteration, but is abandoned due to time restricting reasons. At iteration 3, 5, 19, 21, 22, 23, 24 and 26, it can be seen that the right crack closes. When this happens, the left crack is still open, thus there still is enough energy in the system to stimulate propagation. On the other hand, at iteration 4, 8, 17, 18 and 20 , the left crack closes. it can be seen that when this happens, the right crack is still open, which means again that there still is enough strain energy in the system for crack propagation. After the 27th iteration, the crack grows slightly more to the left than to the right, which corresponds with the literature of the microscope measurements of figure 2.18.

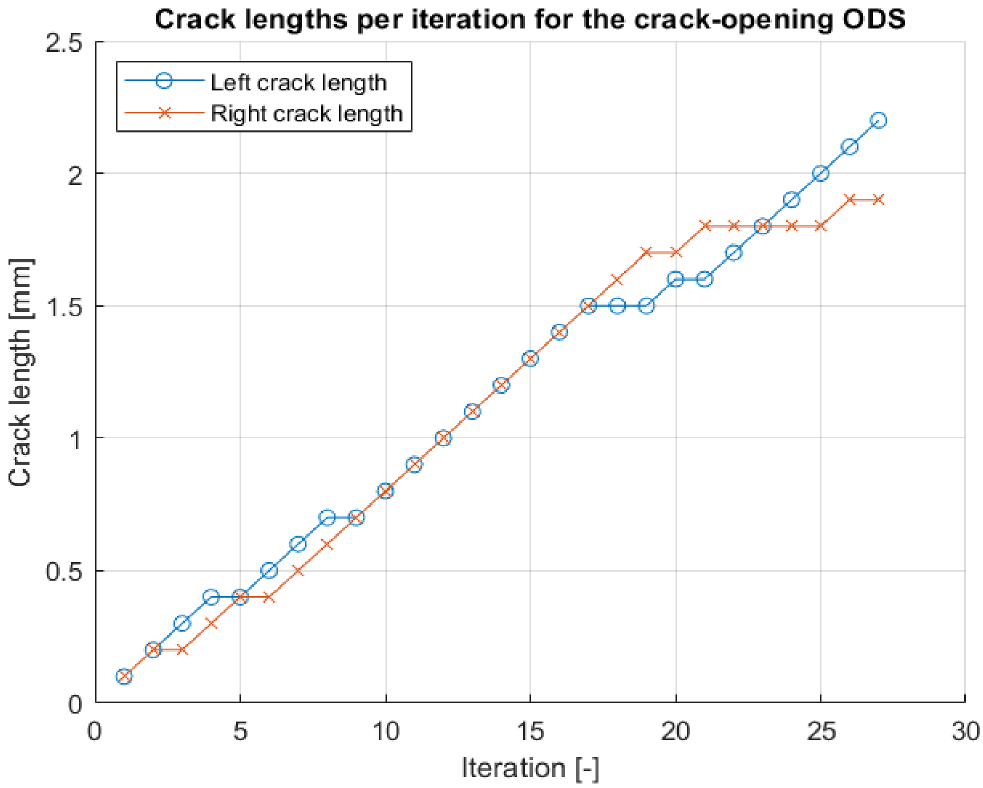

Figure E.1: Crack lengths per iteration for the crack-opening deflection

E.2 Crack growth direction under crack-closing deflection

Whether the crack grows to the right, to the left or in both directions, can be seen in figure E.2. It can be seen that the crack only closes for the right crack at iteration 7. In all the other iterations, the crack opens for both the left and the right side. Until iteration 8. At iteration 8, the crack does not grow in the right direction and it does not grow in the left direction. That means that there is not enough strain energy in the system to open one of the cracks. That is the reason that significantly less iterations are performed for the crack-closing deflection. From iteration 8 on, the crack cannot grow further anymore, as both the left and right crack display no growth anymore. A hypothetical 9th iteration is added, opening one extra node in both directions, to identify what the crack would do. But again, also here, there is not enough strain energy for the crack to grow. It can be seen that after the 8th iteration, the crack grows slightly more to the left than to the right, which corresponds with the literature.

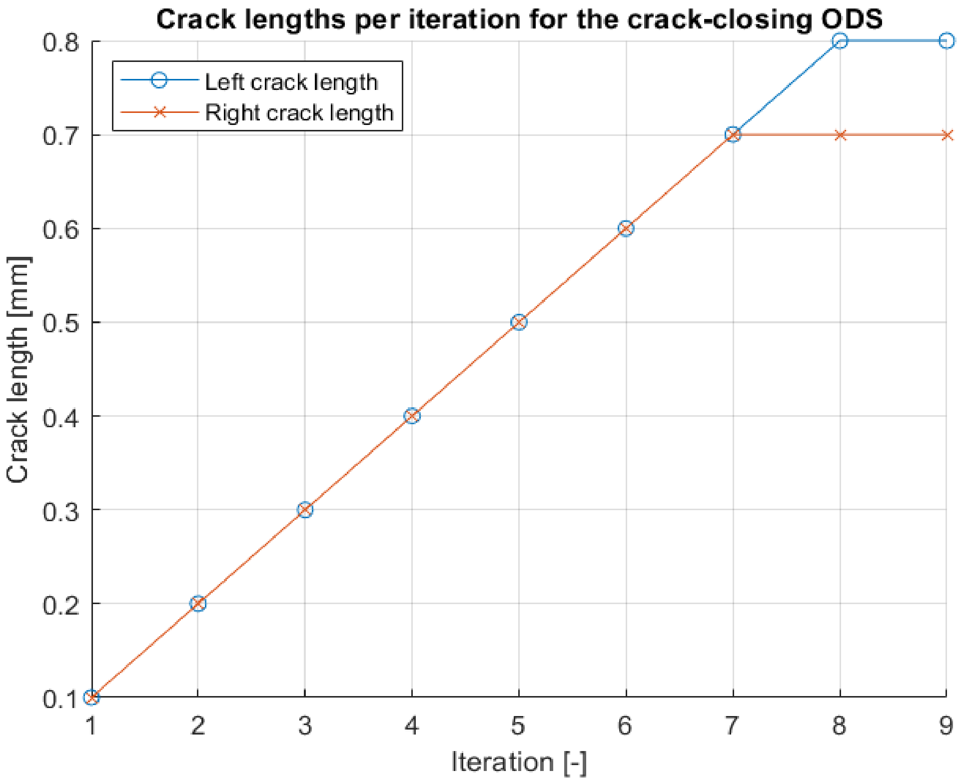

Figure E.2: Crack lengths per iteration for the crack-closing deflection